OSCILLATING SURGE WAVE ENERGY CONVERTER GEOMETRY OPTIMIZATION FOR DIRECT SEAWATER DESALINATION

by

Jason McMorris, B.S., M.S.

May, 2023

Director of Thesis: Faete Filho, Ph.D.
Major Department: Engineering

Abstract

Having a reliable supply of fresh water is a problem that affects nations around the world. Saltwater desalination is one of the best methods for fulfilling this need, but it is an energy-intensive process that is expensive to maintain. Wave energy can be utilized to increase the efficiency of seawater desalination using a wave energy converter (WEC) to lower the external energy requirement. This thesis presents an analysis of scaled down flap-type oscillating surge wave energy converter (OSWEC) geometries and their effects on the power output. The performance of the OSWEC was tested using different flap shapes in addition to different configurations of thickness, density, and center of mass. The tested wave conditions were based on scaled down wave conditions at Jennette's Pier in Nag's Head, North Carolina, and used a significant wave height of 0.117m and a natural period of 1.68s. The system's power take-off (PTO) was also manipulated using different damping and stiffness coefficients to maximize the power generated from the OSWEC. The results of the wave simulations showed that the thinnest configuration of the variable thickness cylindrical flap shape, with the highest tested density and center of mass, produced the most power using the given wave conditions with an average power output of 30.11W.

OSCILLATING SURGE WAVE ENERGY CONVERTER GEOMETRY OPTIMIZATION FOR DIRECT SEAWATER DESALINATION

A Thesis

Presented to the Faculty of the Department of Engineering

East Carolina University®

In Partial Fulfillment of the Requirements for the Degree

Masters of Science in Mechanical Engineering

by

Jason McMorris, B.S., M.S.

May, 2023

OSCILLATING SURGE WAVE ENERGY CONVERTER GEOMETRY OPTIMIZATION FOR DIRECT SEAWATER DESALINATION

by

Jason McMorris, B.S., M.S.

APPROVED BY:

Director of Thesis

Faete Filho, Ph.D.

Committee Member

Tarek Abdel-Salam, Ph.D.

Committee Member

Raymond Smith, Ph.D.

Chair of the Department of Engineering

Barbara Muller-Borer, Ph.D.

Dean of the Graduate School

Kathleen Cox, Ph.D.

Acknowledgements

I would like to thank my supervisor, Dr. Faete Filho, who made this work possible and helped me through all the stages of research and writing. I would also like to thank my committee members for supporting me during my proposal and defense, as well as for giving me insightful suggestions and feedback on how I can improve my work.

I would also like to thank my family for supporting me during my whole school career, especially when I decided to stay an extra year to pursue my masters degree. Your understanding, prayers, and words of encouragement have helped bring me to this point.

Contents

List of Tables

List of Figures

List of Nomenclature

$\ddot{X}$	Translational and rotational vector
ω	Wave frequency
ϕ	Wave phase
ρ	Water density
θ	Wave direction
A	Radiation added mass coefficient
B	Radiation wave damping coefficient
C_{hs}	Linear hydrostatic restoring coefficient
F_B	Net buoyancy restoring force and torque vector
F_m	Mooring connection force and torque vector
F_v	Damping force and torque vector
F_{exc}	Wave excitation force and torque vector
F_{ms}	Morison element force and torque vector
F_{pto}	Power take off force and torque vector

F_{rad} Wave radiation force and torque vector

g Gravity

H Wave height

k Wave number

m Mass matrix

T Wave period

Chapter 1

Introduction

Water scarcity is a pressing global concern, as demand for freshwater continues to increase due to population growth, climate change, and urbanization. Water is an abundant resource, but only 0.5% of Earth's supply is available fresh water.[1] Many coastal regions have much of their freshwater supply contaminated by saltwater, rendering it undrinkable.[2] Desalination, the process of removing salt and other minerals from seawater, is one potential solution to address this challenge. Desalination can provide a reliable and sustainable source of fresh water in areas where traditional sources are scarce or limited. One drawback to desalination is that it is an energy intensive process. One way to reduce or even eliminate the cost of supplying energy for desalination is using renewable energy.[3] Designing renewable energy systems connected to a desalination system is a beneficial long term solution to lower energy costs throughout a desalination plant's lifespan. Because desalination plants are often in close proximity to the ocean in addition to providing high energy density, wave energy is an efficient source of renewable energy. Wave energy is the energy generated by the movement of ocean waves, which can be captured and converted into electricity using various devices, such as oscillating surge wave energy converters (OSWECs).

OSWECs are a type of wave energy converter that utilizes the movement of ocean waves to generate electricity. OSWECs have the potential to provide a renewable and reliable source of energy, and one proposed application is the desalination of seawater. Seawater desalination using renewable energy will lower the cost of running a desalination system, making it a viable source of fresh water with minimized external energy inputs. These renewable desalination plants would provide a decentralized and renewable source of potable water, potentially reducing the need for energy-intensive and greenhouse gas emitting centralized desalination plants. Wave energy can be utilized to increase the efficiency of seawater desalination using a wave energy converter (WEC) combined with a pressure accumulator to convert the wave motion into pressure energy. However, the optimization of OSWEC geometry for desalination has not been extensively studied.

To increase the energy output of the WEC, the geometry of WECs utilizing a rotating flap attached to a fixed base will be manipulated over a range of variables. These variables include the flap shape, thickness, center of mass, and density. The variable related to thickness is dependent on the flap shape; the curve radius, thickness range, cylinder diameter, and cylinder diameter range were manipulated on applicable flap shapes. Another name for OSWECs are terminator WECs. Terminator devices have their principal axis parallel to the wavefront, meaning perpendicular to the predominant wave direction, and physically intercept waves.[4] This motion causes the flap to oscillate, and the mechanical energy will be transferred to the system through a device called the power take-off (PTO). The PTO will transfer the mechanical energy into a pressure accumulator, which will power the reverse osmosis (RO) desalination system. The results were analyzed to determine the design with the highest energy output, and therefore the highest resulting freshwater output from the desalination system.

Chapter 2

Literature Review

2.1 Wave Energy Converters

The global potential for wave energy has been estimated using different models and variables, mainly resulting in values between 1-10 TW (1 TW = 1012 W).[5–7] Wave energy converters (WEC) are one of the leading technologies that use this energy and convert it to other usable forms. WECs are classified into different types by the directional characteristics of their energy absorption; three main types of WECs include point absorbers, attenuators, and terminators. Point absorbers are devices that are either floating on the water's surface or mounted on the seabed and can absorb energy in all directions.[8] Attenuators are another type of WEC that are parallel to the wave direction and oscillate on the wave's surface, converting the mechanical energy of the waves into electrical energy.[8] Terminator WECs are positioned perpendicular to the motion of the waves and absorb energy in one direction. These devices are usually located near the water surface but can be attached to the seafloor at low water depths.[8] A specific type of terminator device is an oscillating surge wave energy converter (OSWEC) consisting of a rotating flap and stationary base. Surge refers to the direction the waves move, which is the same direction the energy will be absorbed, and the

flap will move. An example of an OSWEC device is shown in Figure 2.1 below.[9]

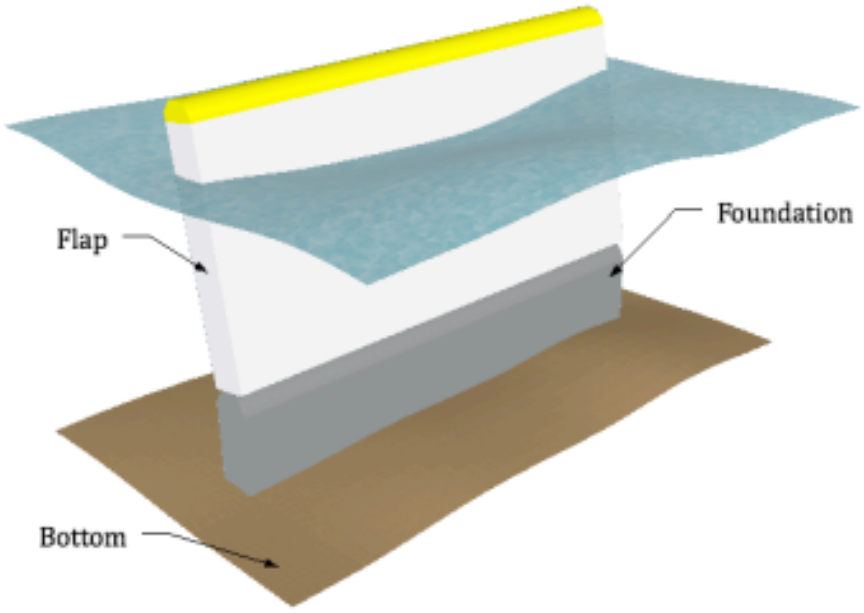

Figure 2.1: Oscillating Surge Wave Energy Converter.

There are multiple ways WEC devices can be used to absorb wave energy due to the variations in shape and size. A study in 2006 proposed a series of point absorbing floating buoys be used with a linear electric energy converter to connect the wave energy to the power grid.[10] A different study completed by Pecher in 2012 used a WEC paired with a smart device to regulate the wave energy absorbed and reduce loads in extreme wave conditions. The device used an A-shaped-slack-moored and floating structure to absorb the wave energy with a series of rotors.[11] Buoys and rotors are different shapes of WEC devices, so the way they absorb the energy of waves is entirely different. The different methods of wave energy conversion can be compared using the magnitude of energy and efficiency.

2.1.1 Wave Powered Desalination

One of the first developments of desalination paired with WEC technology was a plant in Vizhinjam, India. The plant was an onshore autonomous oscillating water column reverse

osmosis plant with a capacity of 150 kW and could produce 10,000 L of freshwater per day. It was created in 1990 and decommissioned in 2011.[12] Other studies have assessed small autonomous desalination units driven by one wave device. One of these proposed reverse osmosis desalination plants was used with a WEC to combat water availability issues and low energy supply due to the limits of living on islands.[13] There is a history of reverse osmosis desalination plants being paired with WEC technology. Studies have demonstrated that RO desalination plants powered by wave energy can operate successfully under variable power over various wave conditions. One study showed that a plant could have a specific energy consumption of less than 2.0 kW h/m3, further supporting this conclusion.[14] This project will use solar energy to power the supercritical water desalination system and wave energy to power the RO system. There are many factors that can impact the efficiency and effectiveness of a WEC. Two main systems that are modified to maximize a WEC's power absorption are the PTO techniques and related variables and the WEC itself. In one study, advanced PTO techniques were used to limit the WEC's rotation so that it would be less likely to become damaged in extreme wave conditions. The goal of this optimization was to avoid the engagement of the brake but keep the amplitude within the specified range.[15] The tests completed in this study were tests on the geometry of the WEC to maximize the power in that way; there are many completed studies using similar methods to design efficient WEC systems.[16,17]

2.1.2 WEC Geometry Optimization

The process of WEC geometry optimization starts with the geometry definition, which will determine the range of possible decision variables that will be manipulated to find the objective metric. An objective function will use decision variables combined with different constraints to calculate viable solutions.[16] A study in 2013 analyzed optimal geometries for wave absorbers oscillating about a fixed axis by using the ratios of the submerged surface area

to maximum absorbed power and the maximum reaction force to the maximum absorbed power over a specified frequency range as cost criteria.[18] The study used a multiobjective optimization algorithm in MATLAB, paired with WAMIT to complete the hydrodynamic diffraction calculations and Multisurf for the geometry design. They concluded that the optimal WEC geometry depends on the wave frequency range. They also determined that most optimal geometries have the axis of rotation close to the sea bottom and the bodies close to the free surface. This study was completed generally, with no specific location in mind and it focused on full-scale devices compared to the scaled down devices in this thesis. Another study used a genetic algorithm to optimize specific parameters of a flap-type WEC including flap width, water depth, and hinge height. This was paired with a semi-analytical model to solve the system hydrodynamics.[9] The study concluded that flap width has a wider range of high quality solutions than the other parameters and the most efficient designs are with smaller flap widths in their test range of 14.6 m to 30 m. A study in 2018 used the design of experiments approach to optimize the geometry of a heaving point absorber WEC.[19] This approach determines how certain variables affect each other while running a minimum number of simulations. In another study, an OSWEC with variable geometry was used to adapt the hydrodynamic properties depending on the sea state to provide more control over the power absorption efficiency and the loads the device was taking on.[20]

2.2 Hydrodynamic Diffraction

To determine the power output of a WEC, the relationship between the waves and the flap must be simulated; this is the hydrodynamic diffraction. The hydrodynamic diffraction results show the resonant behavior of the OSWEC which impacts how much power each design can produce.[21] A number of studies have used different methods to simulate and calculate these relationships, but the majority of them use semi-analytical approaches to

complete these calculations. A particular study used a semi-analytical method to decompose the axisymmetric boundary based on the boundary discretization method. They then used the linear wave theory based on the eigenfunction expansion matching method to obtain the oscillating absorbers and hydrodynamic coefficients.[22] Many WEC designs utilize one of the linear boundary element methods in simulation because they are sufficiently fast to provide the required simulations for this type of application. For more computationally demanding designs, non-linear boundary element methods can be used to maintain calculation speed.[23] For this study, the linear boundary element method will be sufficient to calculate the hydrodynamic coefficients over different flap configurations.

2.2.1 Simulation of a WEC

Different wave conditions and flow models can get data reflecting specific locations and times of the year. WEC simulation technology has developed so that the hydrodynamic coefficients and geometry can be combined and run through an open-source software called WEC-Sim and output different variables based on a user defined function. WEC-Sim can be used for various purposes such as geometrical optimization[16] and design and analysis.[24] WEC-Sim simulations can be validated by comparing the results to that of experimental wave tank tests. In a particular study, the hydrodynamic parameters were obtained, and a heaving point absorber was modeled over multiple buoy shapes and a variety of diameters and drafts that were compared to maximize the power absorption capacity. The procedure also included optimizing the damping coefficient and spring forces to tune the WEC to the wave conditions.[25]

WEC-Sim can also be used to complete free decay tests to determine the natural frequency and damping ratio over different release angles. A study in 2015 used WEC-Sim to simulate the free decay period for the heave and surge directions and compared them to experimental values.[26] A study in 2016 used free decay tests to validate the WEC-Sim

model by comparing experimental and numerical results over different initial displacements. This study normalized the results by the initial displacement to highlight the OSWEC's nonlinear response in the experimental tests. If the response were linear, the normalized decay test results would be independent of the initial displacement.[27,28] In another study, the experimental and numerical responses of an OSWEC in regular waves were compared to each other to validate the system.[29]

Chapter 3

Methodology

3.1 Geometry Design and Optimization

The tested flap shapes were designed in SolidWorks using constraints for a scaled down model to fit in the wave tank at East Carolina University's Coastal Studies Institute. The dimension limitations of the wave tank allowed a maximum flap height of 1.2 meters and a width of 1.5 meters. All of the tested flaps had a standardized height and width to allow the resulting power outputs to be compared to each other. The shapes that were tested include rectangular flap, a curved surface flap, a variable thickness flap, a cylindrical flap, and a variable diameter cylindrical flap. Using Figure 7.2, the flap thickness refers to the variable on the x-axis, the dimension in the right view of the part. The flap width refers to the variable on the y-axis and the flap height refers to the variable along the z-axis. Drawings of the other flap shapes with the same references for the thickness related variable, height, and width can be seen in the Appendix.

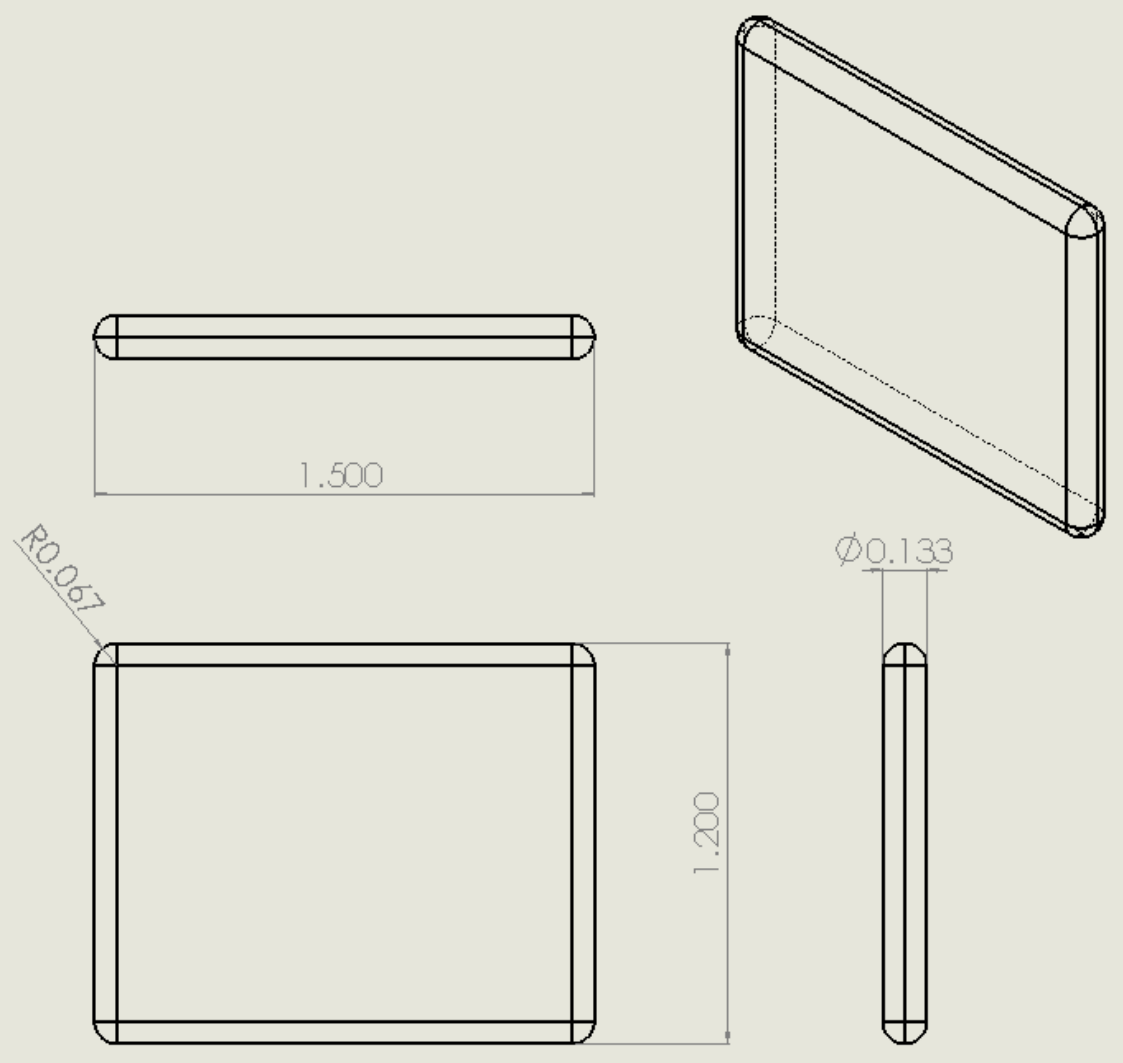

Figure 3.1: Rectangular Flap Drawing.

Each shape had one variable relating to the thickness of the flap that was tested over different values in addition to every shape being tested with different center of masses and densities. All of the flaps were tested under three different density values as well as center of mass locations. The density values were based on the density of seawater, being 20%, 40%, and 60% of the total seawater density. The center of mass values tested included the natural center of gravity, as well as 0.18 meters up and down from the default center of gravity, which is 15% of the total flap height. Each of the flaps were also tested using a variable related

to the thickness, but varied depending on the shape. The rectangular flap was tested using thickness, the curved surface flap was tested using the curve radius, the variable thickness flap was tested using the thickness range, the cylindrical flap was tested using the cylinder diameter, and the variable thickness cylindrical flap was tested using the diameter range. Table 3.1 below shows the thickness related variables for each shape and the tested values.

Table 3.1: Thickness Related Variables and Tested Values

Flap Shape	**Thickness Related Variable**	**Test 1**	**Test 2**	**Test 3**
Rectangular	Thickness (m)	0.05	0.1333	0.2167
Curved Surface	Curve Radius (m)	0.025	0.0667	0.1083
Variable Thickness	Thickness Range (m)	0.15-0.18	0.15-0.2167	0.15-0.2583
Cylindrical	Cylinder Diameter (m)	0.19375	0.241667	0.28
Variable Thickness Cylindrical	Cylinder Diameter Range (m)	0.1-0.2875	0.15-0.333	0.2-0.36

3.2 Mesh Generation

Rhinoceros 3D (Rhino) is a computer aided design software that specializes in producing a mathematically precise representation of curves and freeform surfaces.[30] Rhino can generate a quadrilateral mesh, also called structured mesh, which provides more accurate results than a triangular mesh at higher-order schemes. SolidWorks also has the capability to generate meshes but can only create triangular meshes. The SolidWorks part file from each design was input into Rhino and the created mesh was used as an input for the boundary element method software to calculate the hydrodynamic coefficients. A visualization for the quadrilateral mesh of the rectangular flap can be seen in Figure 3.2 and the meshes for all of the shapes together can be seen in the Appendix.

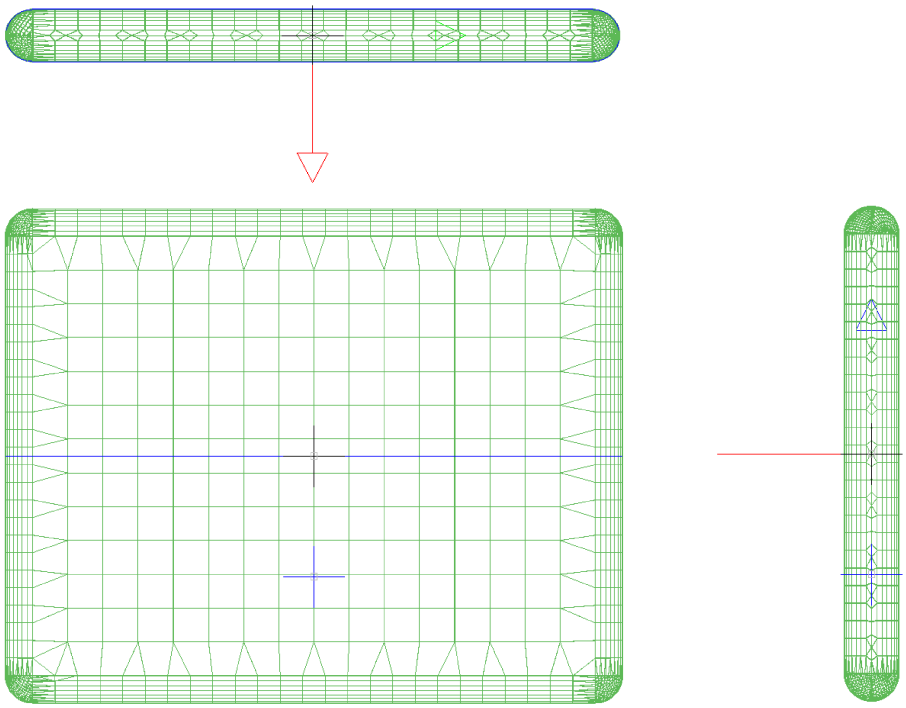

Figure 3.2: Rectangular Flap Mesh Visualization.

The number of quadrilateral panels in the meshes varied for each shape and configuration, but all were above 2000 elements for the hydrodynamic diffraction as a baseline for the level of mesh resolution. The meshes were created using ".step" files exported from SolidWorks, which are NURBS objects. This means that the flaps were modeled with points that were connected by curves. The NURBS objects were transformed into meshes using Rhino's polygon meshing options and NURBS meshing parameters. These parameters include the density, maximum angle, maximum aspect ratio, minimum edge length, maximum edge length, maximum distance, edge to surface, and minimum initial grid quads. The values for these parameters were 1.0, 0.0, 10.0, 0.0001, 0.0, and 0.0, respectively. The minimum initial grid quads was different for each mesh, and was dependent on the flap size/surface area and the amount of time the hydrodynamic simulations took. The meshes were refined using a built in function in Rhino; Rhino uses a recursive process to refine the mesh by subdividing

quadrangles until they meet the criteria defined by the maximum angle, minimum edge length, maximum edge length, and maximum distance, edge to surface options.

3.3 Hydrodynamic Simulation

The hydrodynamic coefficients were calculated using a boundary element software called WAMIT. The hydrodynamic coefficients are what characterize the relationships between the WEC and the ocean waves. Individual simulations were completed for each flap shape, the shape dependent variable, and the center of mass. The center of mass was changed by translating the flap along the z-axis in the mesh file, in which the center of mass is stored as the origin and correcting the translation in the WAMIT simulation. For example, to translate the center of mass down by 0.18m, the location of the flap in Rhino was translated up 0.18m so the origin was located lower on the flap. To correct the flap location for WAMIT, the flap was translated down by the original distance from the top of the flap to the center of mass plus the added 0.18m to put the whole flap below the waterline. The WEC configuration for the mesh generation and hydrodynamic diffraction calculations can be seen in Figure 3.3.

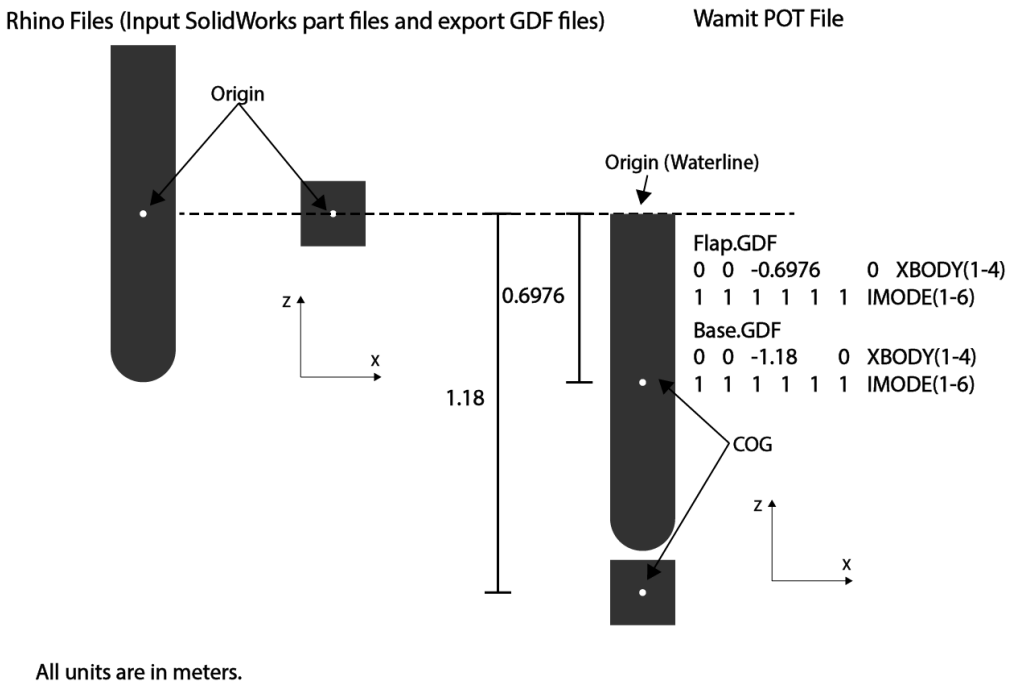

Figure 3.3: WEC Setup for Hydrodynamic Analysis.

The output files from the WAMIT simulations were run through a boundary element method input/output (BEMIO) code to preprocess the data for WEC-Sim, where the WAMIT output files were converted into ".h5" files that were read by WEC-SIM. The hydrodynamic simulation potential control file was set up so that the water depth was 1.4m, the radiation velocity potentials due to all six rigid-body modes of motion were calculated, 502 wave periods were analyzed, and 10 wave angles were in increments of 10 degrees. The potential control file is also where the flap and base mesh files were set and translated so they were below the waterline. The hydrodynamic simulation configuration file was set up using WAMIT's iterative solver, meaning the simulations were much faster for completing simulations with large systems of equations. The force control file was set up so that it included the added-mass and damping coefficients. The force control file was also set up so that it output the exciting forces and also the separate Froude-Krylov and scattering components of these forces.

3.4 Simulating a WEC

WEC-Sim was used to calculate the power output from the different flap geometries. This software scales the hydrodynamic coefficients according to the variables in Equations 3.1-3.4 below

$$|F_{exc}(\omega) = \frac{|F_{exc}(\omega)}{\rho g}| \tag{3.1}$$

$$A(\omega) = \frac{A(\omega)}{\rho}| \tag{3.2}$$

$$B(\omega) = \frac{B(\omega)}{\rho\omega}| \tag{3.3}$$

$$C_{hs} = \frac{C_{hs}}{\rho g}| \tag{3.4}$$

where ρ is the water density, ω is the wave frequency in rad/s, g is gravity, F_{exc} is the wave-excitation force and torque vector, A is the radiation added mass coefficient, B is the radiation wave damping coefficient, and C_{hs} is the linear hydrostatic restoring coefficient.[31] After scaling the hydrodynamic coefficients, WEC-Sim solves the time domain equation of motion for a floating body about its center of gravity, as shown in Equation 3.5

$$(m)\ddot{X} = F_{exc}(t) + F_{rad}(t) + F_{pto}(t) + F_v(t) + F_{me}(t) + F_B(t) + F_m(t) \tag{3.5}$$

where $\ddot{X}$ is the translational and rotational acceleration vector of the device, m is the mass matrix, $F_exc(t)$ is the wave excitation force and 6-element torque vector, $F_rad(t)$ is the force and torque vector resulting from wave radiation, $F_{pto}(t)$ is the PTO force and torque vector, $F_v(t)$ is the damping force and torque vector, $F_{me}(t)$ is the Morison Element force and torque vector, $F_B(t)$ is the net buoyancy restoring force and torque vector, and $F_m(t)$ is the force and torque vector resulting from the mooring connection.[31]

The WEC-Sim file used the input files from SolidWorks and WAMIT, ran a user-defined

function, and repeated for each geometry over the variable ranges. The user-defined function was written to give multiple outputs including power output, natural period, and angular position in the various tests. The WEC models were tested under regular wave conditions based on the wave conditions at Jennette's Pier in Nags Head, NC. The equation for regular incident waves is defined in Equation 3.6.

$$\eta(x, y, t) = \frac{H}{2} \cos(\omega t - k(x \cos\theta + y \sin\theta) + \phi) \tag{3.6}$$

Regular waves are defined as sinusoidal waves where H is the wave height, ω is the wave frequency ($\omega = \frac{2\pi}{T}$), k is the wave number ($k = \frac{2\pi}{\lambda}$), θ is the wave direction, and ϕ is the wave phase.[31]

The mean power output values were calculated over a matrix of PTO stiffness and damping values to find the maximum output for each geometry configuration combined with the wave values. An example power matrix can be seen in Table 3.2 below.

Table 3.2: Rectangular Flap Damping and Stiffness Power Matrix

Stiffness (K), Nm/rad	15500	-19.0148	-25.8266	-27.8619	-27.9101	-27.1191	-25.9922	-24.7599	-23.5292
	15000	-19.8567	-26.5896	-28.4478	-28.3481	-27.4485	-26.2437	-24.9551	-23.6832
	14500	-20.6116	-27.2548	-28.9503	-28.7201	-27.7264	-26.4548	-25.1184	-23.8117
	14000	-21.2505	-27.8039	-29.3594	-29.0203	-27.9493	-26.6235	-25.2485	-23.9139
	13500	-21.746	-28.2207	-29.6662	-29.2438	-28.1146	-26.7482	-25.3445	-23.9892
	13000	-22.0748	-28.492	-29.8639	-29.3869	-28.22	-26.8275	-25.4054	-24.0369
	12500	-22.2204	-28.609	-29.9479	-29.4473	-28.2642	-26.8607	-25.4309	-24.0568
	12000	-22.175	-28.5677	-29.9163	-29.4238	-28.2467	-26.8473	-25.4206	-24.0488
	11500	-21.9406	-28.3694	-29.7698	-29.3168	-28.1675	-26.7876	-25.3746	-24.0128
	11000	-21.5287	-28.0204	-29.5116	-29.1282	-28.0278	-26.6822	-25.2934	-23.9491
	10500	-20.959	-27.5318	-29.1476	-28.861	-27.8294	-26.532	-25.1776	-23.8582
	10000	-20.257	-26.9182	-28.6856	-28.5197	-27.5747	-26.3387	-25.0282	-23.7406
	9500	-19.4514	-26.1972	-28.1352	-28.1095	-27.2668	-26.1041	-24.8463	-23.5973
Time Step = 0.01 s		500	1000	1500	2000	2500	3000	3500	4000
		Damping (C), Nsm/rad							

The WEC-Sim simulation used an ".stl" file created with SolidWorks and Rhino to show

a visualization of the flap responding to the waves in addition to the output file supplied by WAMIT called the mechanics explorer. This visualization was used to verify that the WAMIT and WEC-Sim simulations were run correctly, and the results made sense by confirming that the flap rotations matched with the expected flap reactions to the waves. With all of the chosen variables, the power output was calculated for five flap shapes over three variations of the thickness-related parameter, with three center of mass values for each thickness-related configuration, and all the other variables tested over three density values.

3.5 Free Decay

A no-wave case was simulated on the rectangular flap to perform free decay tests which were used to determine the natural frequency, ω_n, by displacing the flaps and releasing them and observing how long it takes the flap to come to rest. The free decay tests were completed for the three geometries of rectangular flaps using the initial center of mass and lowest density value to compare to the experimental results obtained using a flap of similar geometry in the wave tank at ECU's Coastal Studies Institute. This was completed in WEC-Sim using a wave configuration that simulates no waves, setting an initial flap angle, and removing the PTO stiffness and damping.

The flaps were simulated under multiple angles to determine a trend between the period of oscillation and angular position. The angles were chosen by taking the angle of the experimental flap right before it was released in each test. To compare the experimental data with the simulated data, one period of the experimental data was taken for each initial angle and plotted. The experimental initial angles were measured and used to run simulations for each of the rectangular flaps. The natural period for each simulation was taken for ten oscillations and averaged to get a value that accurately represents the simulation data.

3.5.1 Experimental Free Decay Setup

Five free decay tests were taken using the experimental flap in the wave tank at the Coastal Studies Institute. The wave tank is 12m long, 3.2m wide, and 1.7m tall with a 12mm steel frame. The wave tank was designed to model a 1:50 to 1:100 scale of the North Atlantic seas. The novotechnik, NOVOHALL Rotary Sensor touchless technology transmissive Series RFC-4800 sensor was used to measure the angular position of the flap. This device has an electrical range up to 360° and has resolution up to 14 Bit. The sensor is a mechanically decoupled 2-part device that can function within $-40°C$ to $125°C$. The sensor output the date/time in addition to the angular position of the flap and it output a measurement every 0.01s during the tests. A possible source of error and uncertainty is from the water bouncing back off of the wave tank and into the flap, changing the natural period of the flap. Another source of possible error and uncertainty is from not holding the flap still at the initial angle for long enough for the water to completely settle. The initial movement of the water would affect the free decay of the flap.

Chapter 4

Results and Analysis

4.1 Power Matrices

The power matrix simulations showed that the flap shape providing the highest power output was the variable thickness cylindrical design with a value of 30.106W produced. The tested variable values for this power output were 60% seawater density, smallest cylinder diameter variation from the bottom to the top of the device, and center of mass moved up 0.18m from the original center of mass. The variable thickness cylindrical flap shape had the highest average power over all variable configurations, with a minimum power generated of 30.059W. The remaining flap shapes provided the greatest to least power in the following order: cylindrical, curved surface, rectangular, and variable thickness. The variable thickness flap had power outputs much lower than the other shapes with a peak mean power generated of 29.913W. The only other flap shape besides the variable thickness cylindrical flap to provide a mean power greater than 30W was the cylindrical flap. The thickness related variable caused power variations between 0.03 and 0.1W. The density and center of mass caused variations less than 0.01W. The power data can be better visualized in a series of graphs to show the relationship of the different tested variables to the produced power. The

simulation generated power outputs for each flap configuration for 400 seconds and over a range of PTO stiffness and damping values; the data values shown in the following graphs are the mean power produced during the 400 seconds with the most effective PTO stiffness and damping values for each configuration of flap shape, thickness, density, and center of mass. The power output of the rectangular flap for the three thicknesses tested, with a set of data for each tested density can be seen in Figure 4.1.

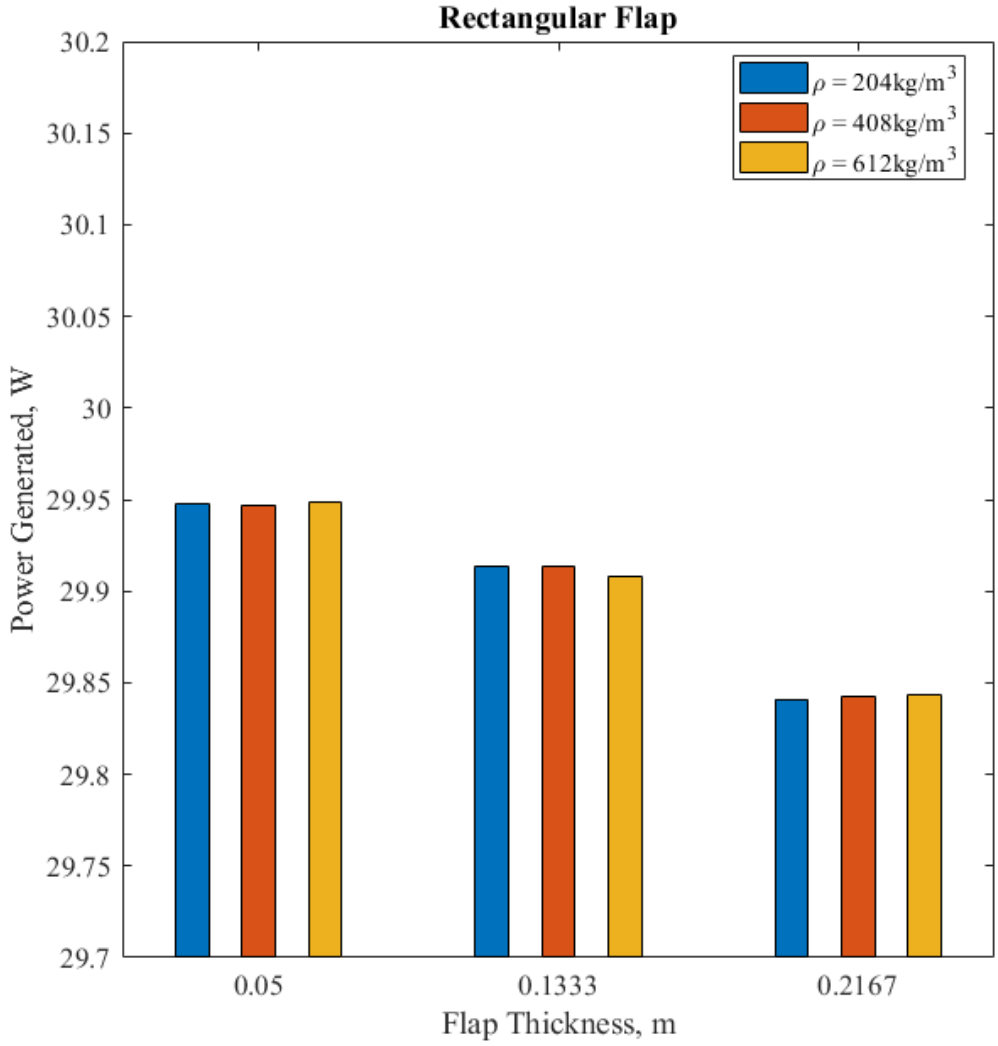

Figure 4.1: Rectangular Flap Power Output Over Different Thicknesses and Densities.

As the rectangular flap got thicker, the power output decreased. The mean power produced at a thickness of 0.05m produced an average of 29.9478W with a range of 0.0012W over the tested densities. The most significant change in power output caused by the density change was using a thickness of 0.1333m with a range of 0.0057W and an average mean of 29.9118W produced over the tested densities. The rectangular flaps the highest thickness, 0.2167m, produced significantly less power than the thinner flaps with an average limit of 29.8422W generated. The flaps with a thickness of 0.05m had mean power outputs that were 0.1057W more than the thickest flaps averaged over the tested densities. The power output of the curved surface flap for the three curve radii tested, with a data set for each tested density can be seen in Figure 4.2.

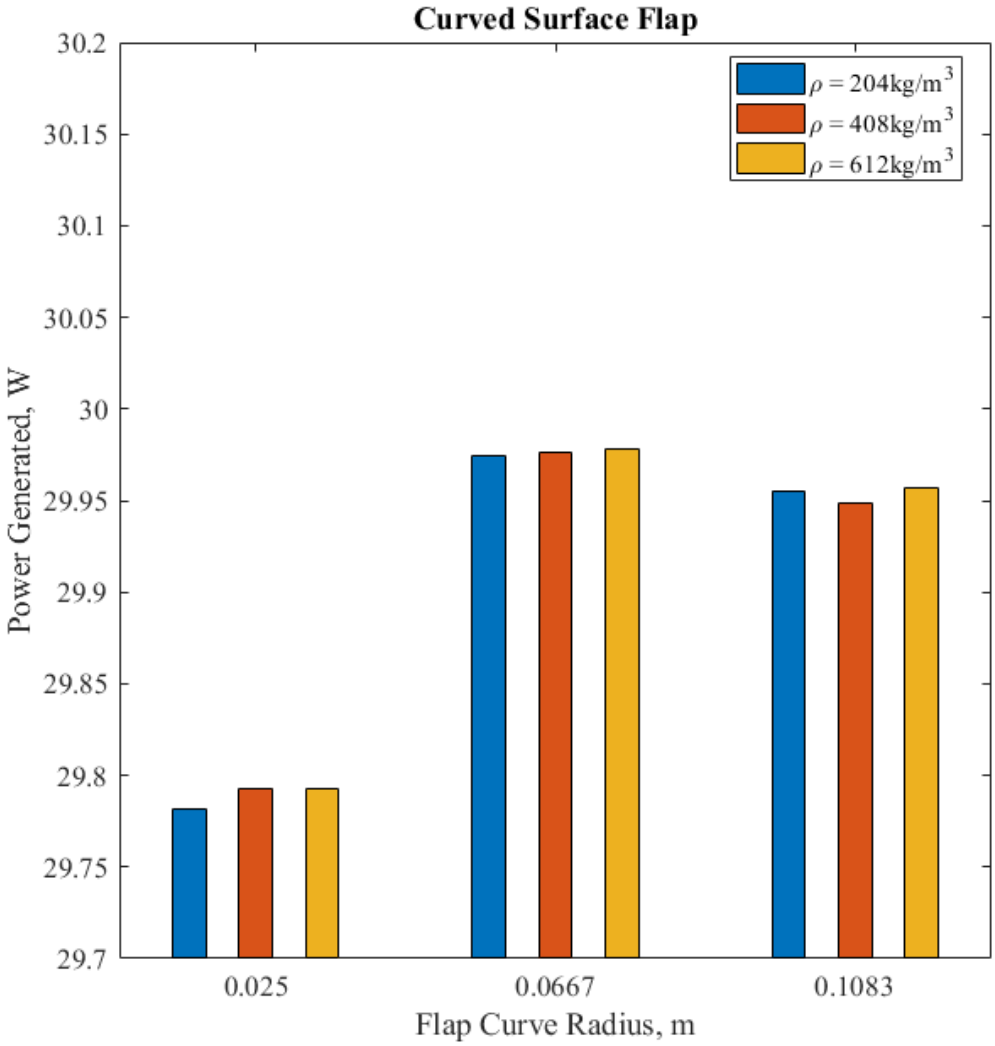

Figure 4.2: Curved Surface Flap Power Output Over Different Curve Radii and Densities.

The curved surface flap had the highest mean power output when using a curve radius of 0.0667m with an average of 29.9762W over the densities tested. Testing different density values created no trends in the power output between the different flap curve radii. The flaps with a curve radius of 0.1083m generated an average mean power of 29.9538W over the tested densities and the flaps with a curve radius of 0.025m generated an average mean power of 29.789W over the tested densities. The lowest curve radius produced mean power

outputs that were significantly lower than the results of the thicker flaps. The difference in power was 0.1871W between the most efficient and least efficient thicknesses, averaged over the tested densities. The power output of the variable thickness flap for the three thickness ranges tested, with a data set for each tested density can be seen in Figure 4.3.

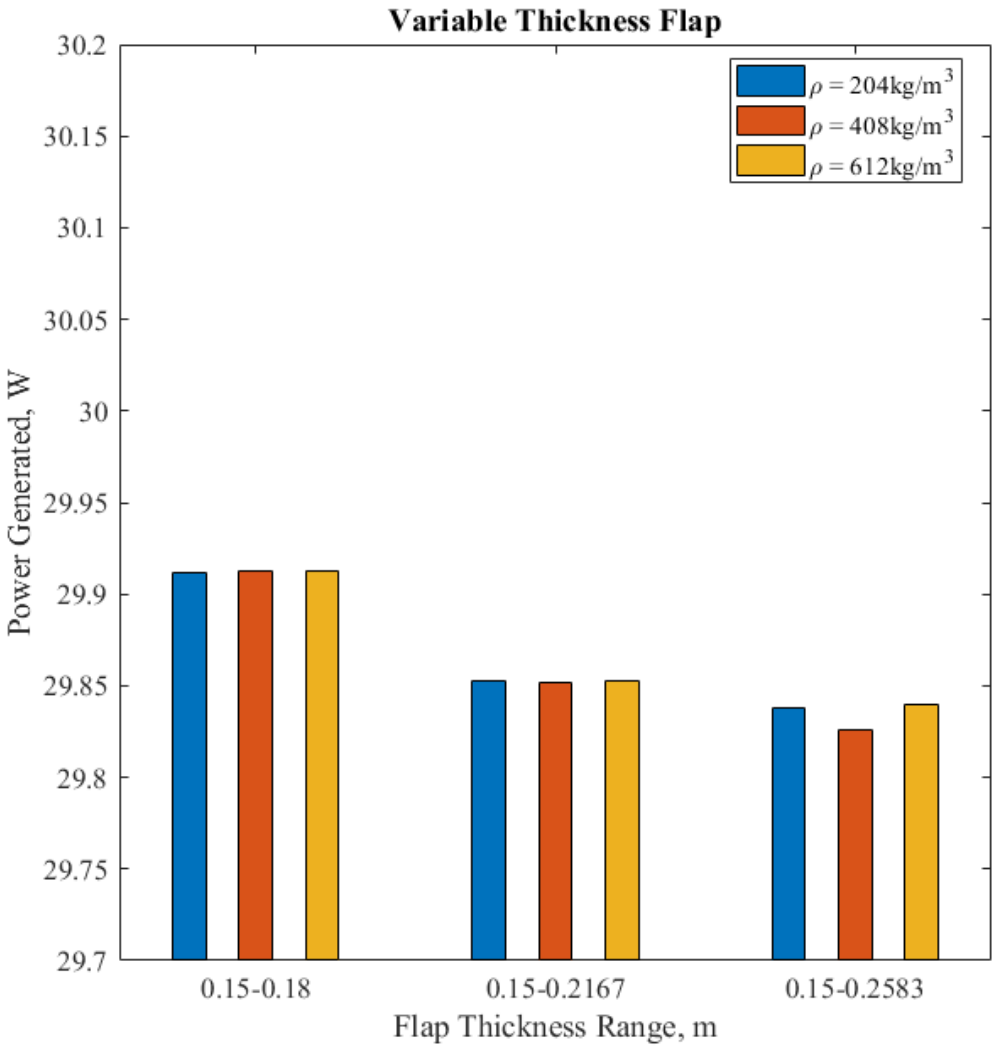

Figure 4.3: Variable Thickness Flap Power Output Over Different Thickness Ranges and Densities.

The variable thickness flap followed the same trend as the rectangular flap as the power generated decreased as the flap thickness range increased. The mean power generated over the flap thickness ranges from least to greatest, and averaged over the density tests, were 29.9125, 29.8523, and 29.8346 respectively. The most significant change in generated power for the change in density was between $408kg/m^3$ and $612kg/m^3$ in the highest thickness range with a difference of 0.01356W. The power output of the cylindrical flap for the three cylinder diameters tested, with a data set for each tested density can be seen in Figure 4.4.

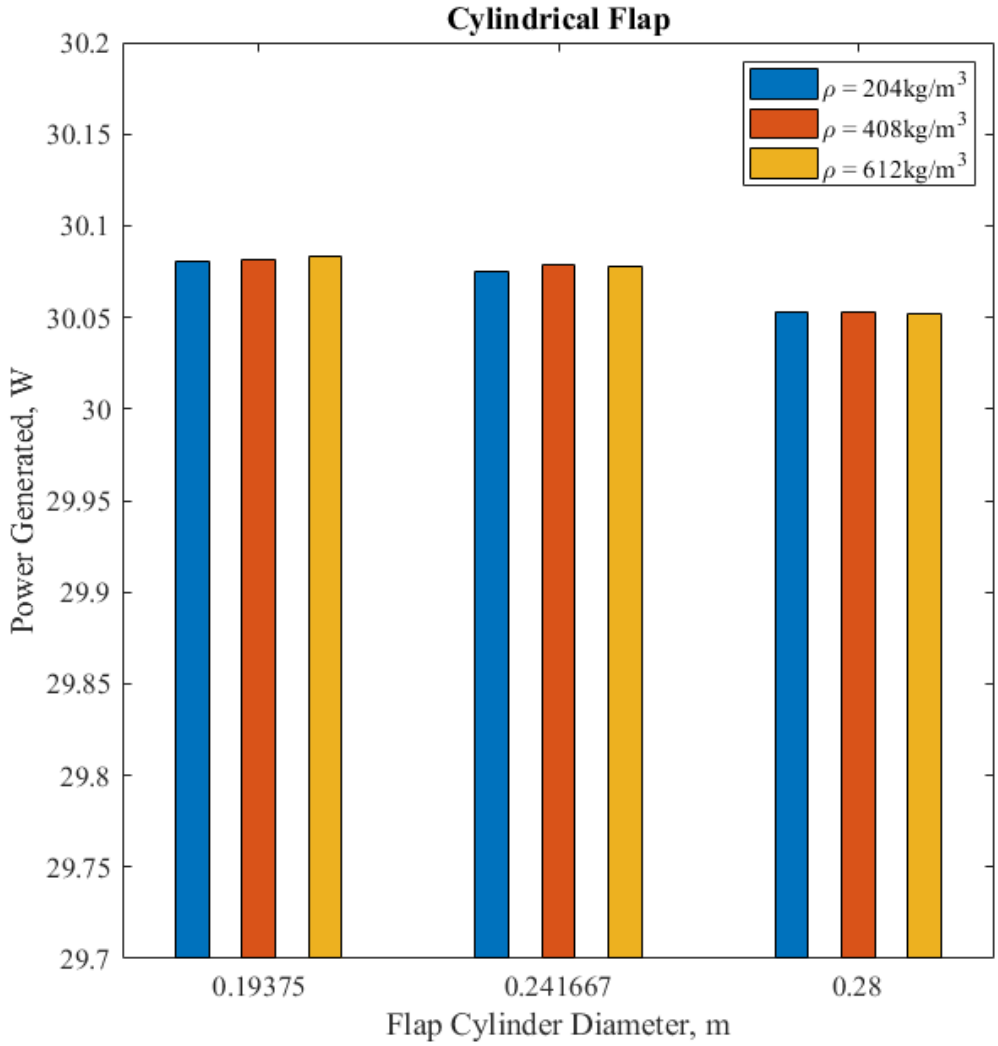

Figure 4.4: Cylindrical Flap Power Output Over Different Cylinder Diameters and Densities.

The mean power output of the cylindrical flaps followed the trend that the thinnest variation produced the most power and decreased as the flap cylinder diameter increased. The range of mean power generation values was small, with the highest mean power coming from the densest flap of the thinnest configuration with a value of 30.0829W and the lowest mean power coming from the densest flap of the thickest configuration with a value of 30.0523W. The density of the flaps at each cylinder diameter variation did not follow a

trend and caused mean power output changes less than 0.01W. The power output of the variable thickness cylindrical flap for the three diameter ranges tested, with a data set for each tested density can be seen in Figure 4.5.

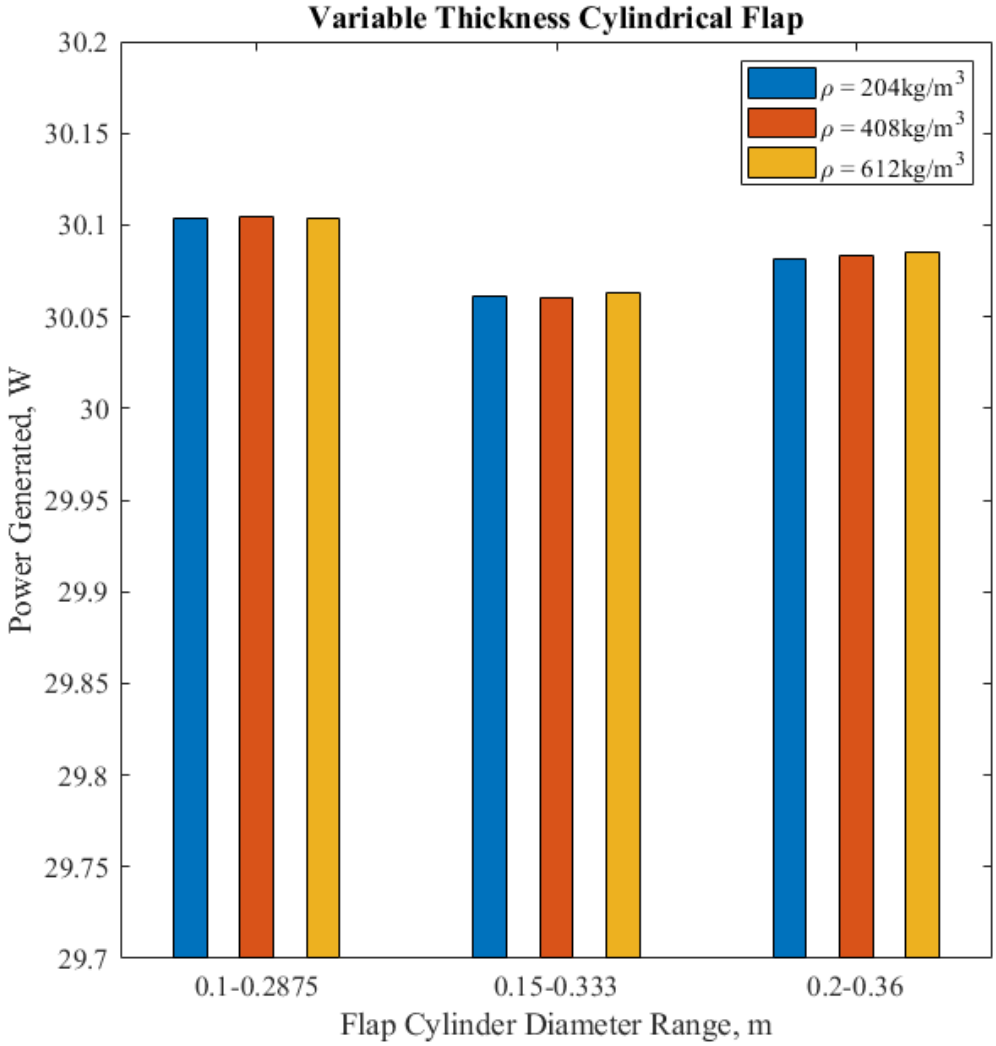

Figure 4.5: Variable Thickness Cylindrical Flap Power Output Over Different Cylinder Diameter Ranges and Densities.

The maximum power generated by the variable thickness cylindrical flaps had an average output of 30.1037W for a thickness range of 0.1-0.2875m, an average output of 30.0615W for a thickness range of 0.15-0.333m, and an average output of 30.0834W for a thickness range of 0.2-0.36m, averaged over the tested densities. The density changes did not cause any trends or significant changes in the generated power for this flap shape. The power output of the rectangular flap for the three thicknesses tested, with a data set for each tested center of mass can be seen in Figure 4.6.

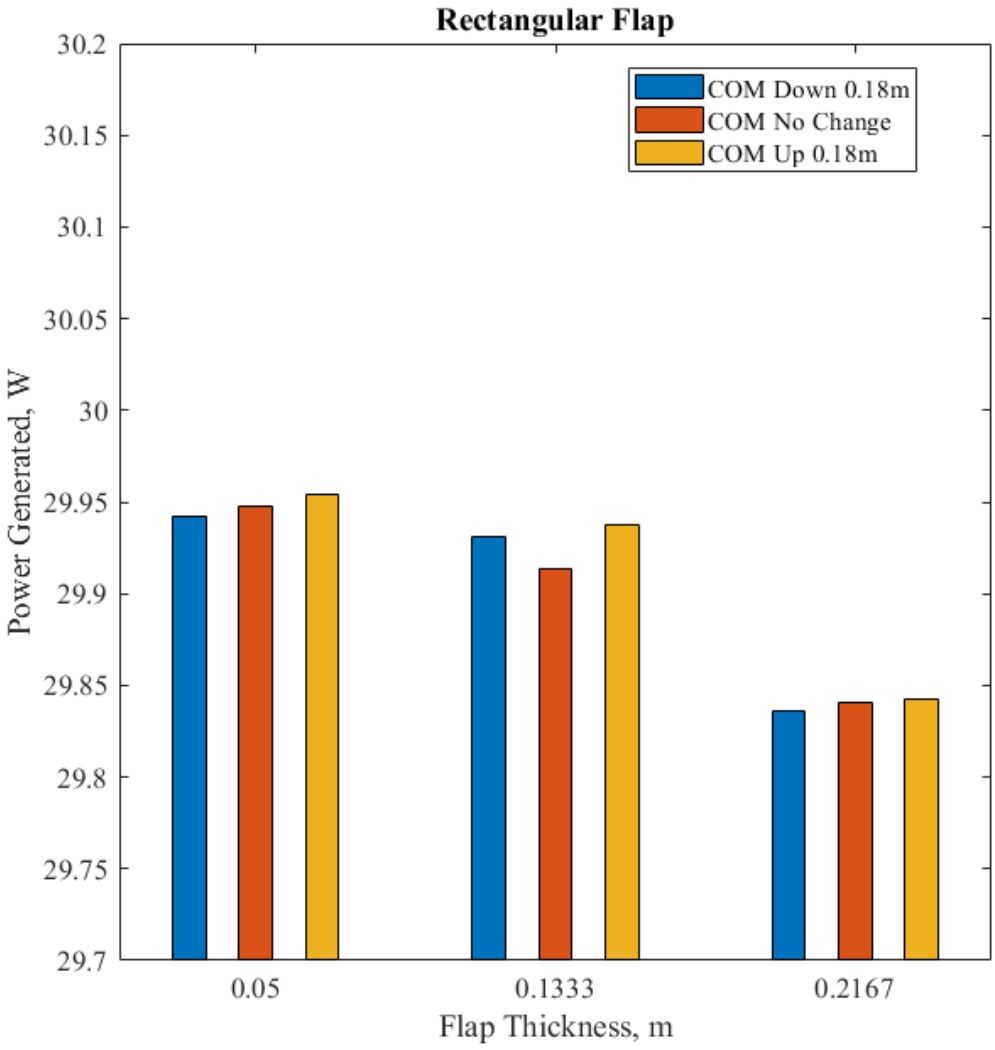

Figure 4.6: Rectangular Flap Power Output Over Different Thicknesses and COMs.

The mean power output for the rectangular flaps generally increased as the center of mass was moved up, with an outlier under the thickness of 0.1333m and no center of mass change. The peak generated power increased from the lowest to highest center of mass by 0.01224W for a thickness of 0.05m, by 0.00668W for a thickness of 0.1333m, and by 0.00693W for a thickness of 0.2167m. The power output of the curved surface flap for the three curve radii tested, with a data set for each tested center of mass can be seen in Figure 4.7.

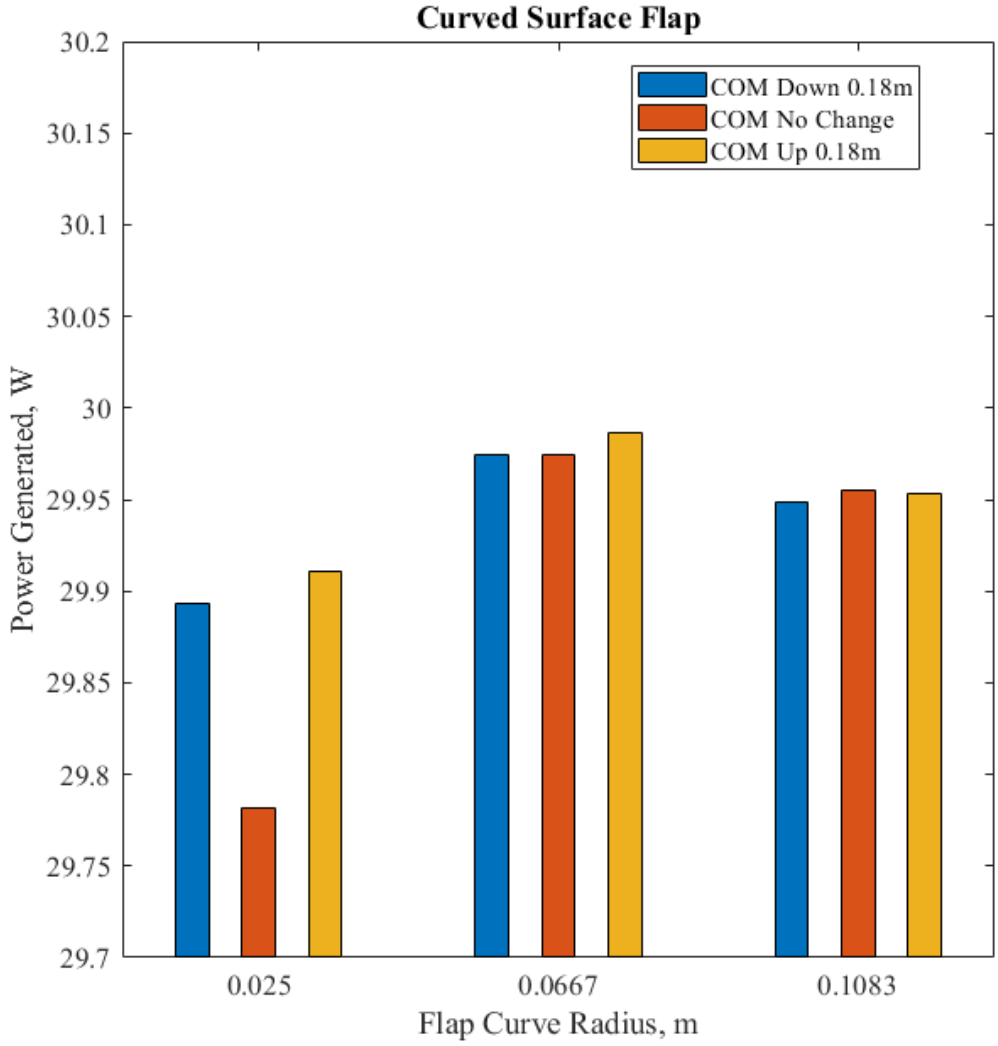

Figure 4.7: Curved Surface Flap Power Output Over Different Curve Radii and COMs.

The mean power output for the curved surface flaps generally increased as the center of mass was moved up, with an outlier under the thickness of 0.025m and no center of mass change where the maximum produced power was significantly lower than the other tests. The power output was significantly lower for all of the tested densities of the lowest thickness, no center of mass change configuration of the curved surface flap. These three configurations produced around 29.78W. The cause of the lower power output could be due to an error or irregularity in the geometry files used in the hydrodynamic simulations as all of the settings in the WEC-Sim simulation were the same as the other tests, but the exact cause of these outliers was not found. The mean power generated was the highest at the highest center of mass for the 0.025m and 0.0667m curve radii tests but was the highest in the middle center of mass value for the 0.1083m curve radius test. The mean power generation values between the lowest and highest center of masses for the 0.025m and 0.0667m curve radii increased by 0.01814W and 0.01213W, respectively. The difference in mean power generation values between the lowest center of mass and middle center of mass for the thickness of 0.1083m was 0.00709W. The power output of the variable thickness flap for the three thickness ranges tested, with a data set for each tested center of mass can be seen in Figure 4.8.

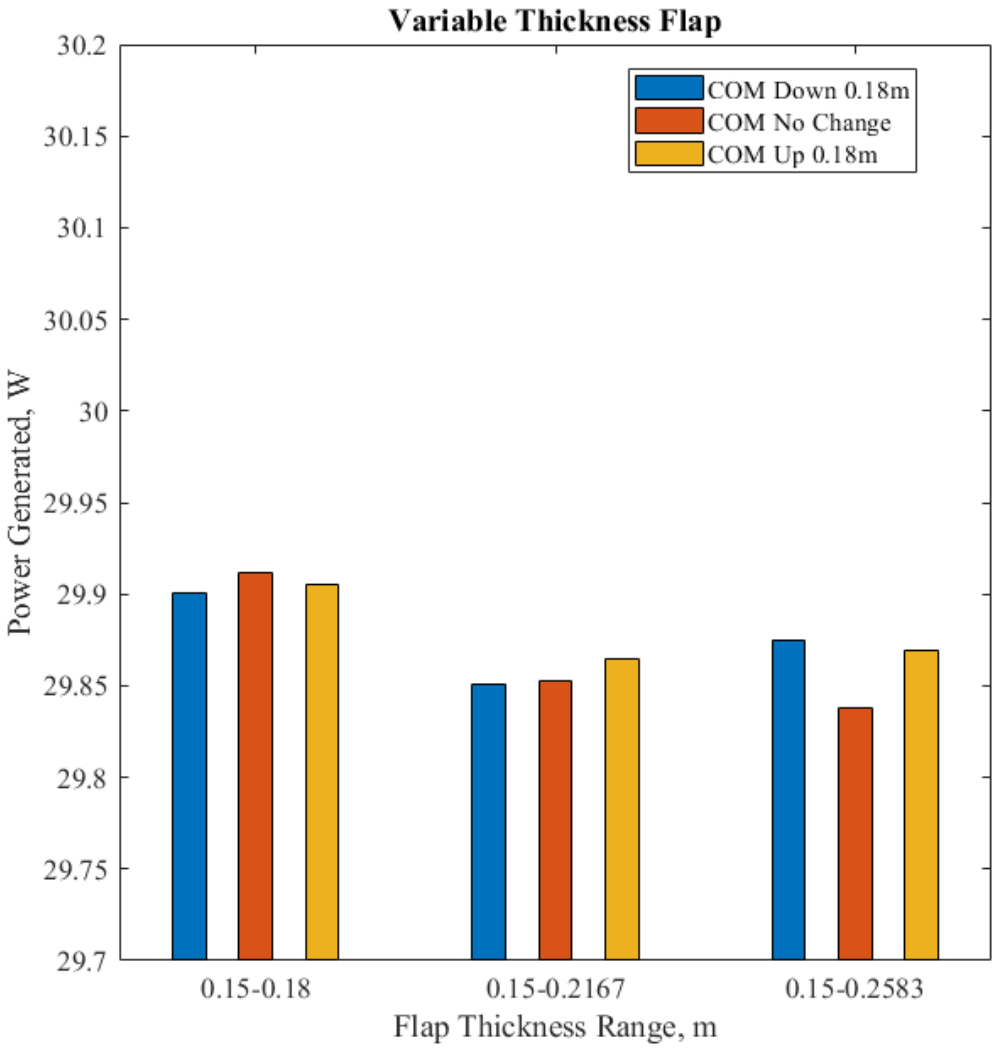

Figure 4.8: Variable Thickness Flap Power Output Over Different Thickness Ranges and COMs.

The mean power output for the variable thickness flap showed no trend over the center of mass changes between the different thicknesses. The generated power was the highest for the thickness range of 0.15-0.18m under no change of the center of mass with and a value of 29.9119W. The generated power was the highest for the thickness range of 0.15-0.2167m using a center of mass translation up 0.18m with and a value of 29.8647W. The generated power was the highest for the thickness range of 0.15-0.2583m using a center of

mass translation down 0.18m with and a value of 29.8749W. The power output variations over the center of masses were 0.011W, 0.0136W, and 0.0371W from the lowest to highest thickness ranges. The power output of the cylindrical flap for the three cylinder diameters tested, with a data set for each tested center of mass can be seen in Figure 4.9.

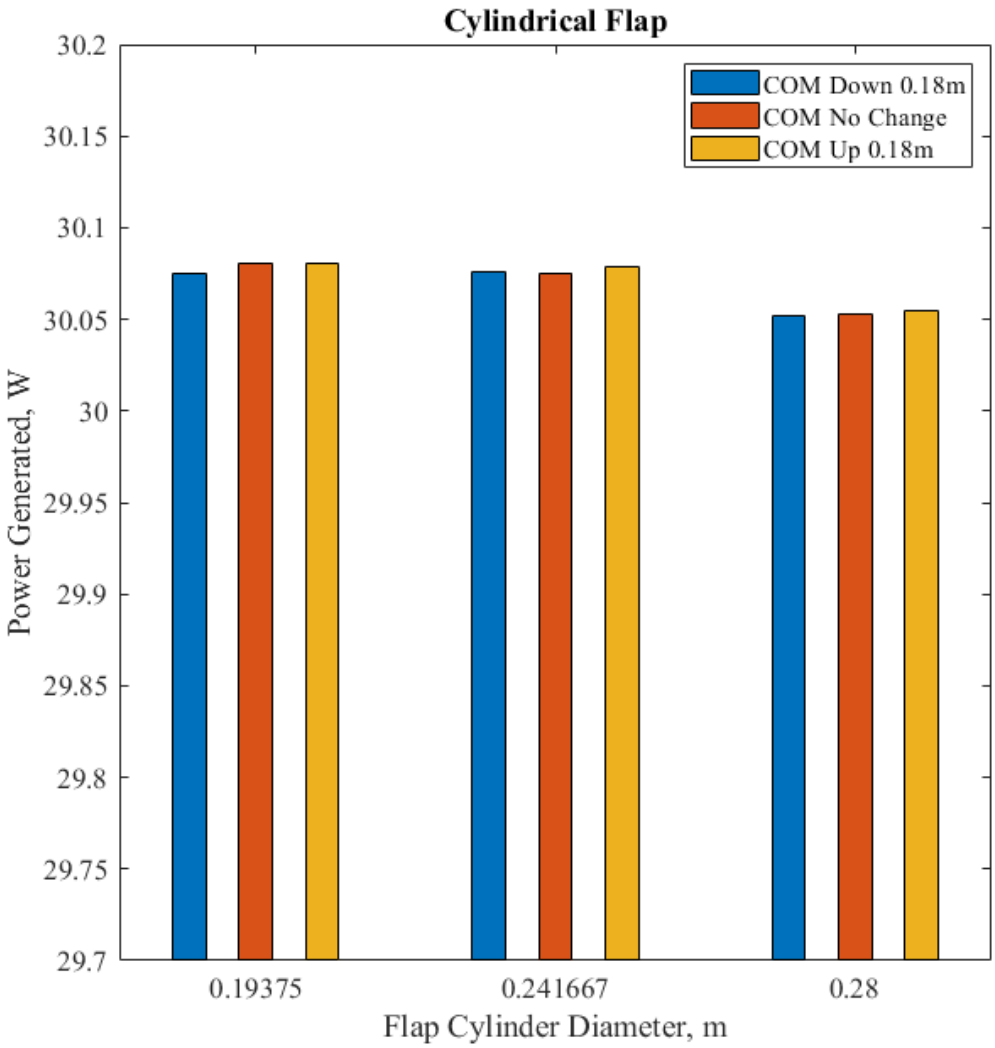

Figure 4.9: Cylindrical Flap Power Output Over Different Cylinder Diameters and COMs.

The mean power generated for the cylindrical flaps were the highest when the center of mass was translated up and the lowest when the center of mass was translated down. The power output increased by 0.00515W for a cylinder diameter of 0.19375m, by 0.00278W for a cylinder diameter of 0.241667m, and by 0.0034W for a cylinder diameter of 0.28m as the center of mass was translated from the lowest to highest point. The power output of the variable thickness cylindrical flap for the three cylinder diameter ranges tested, with a data set for each tested center of mass can be seen in Figure 4.10.

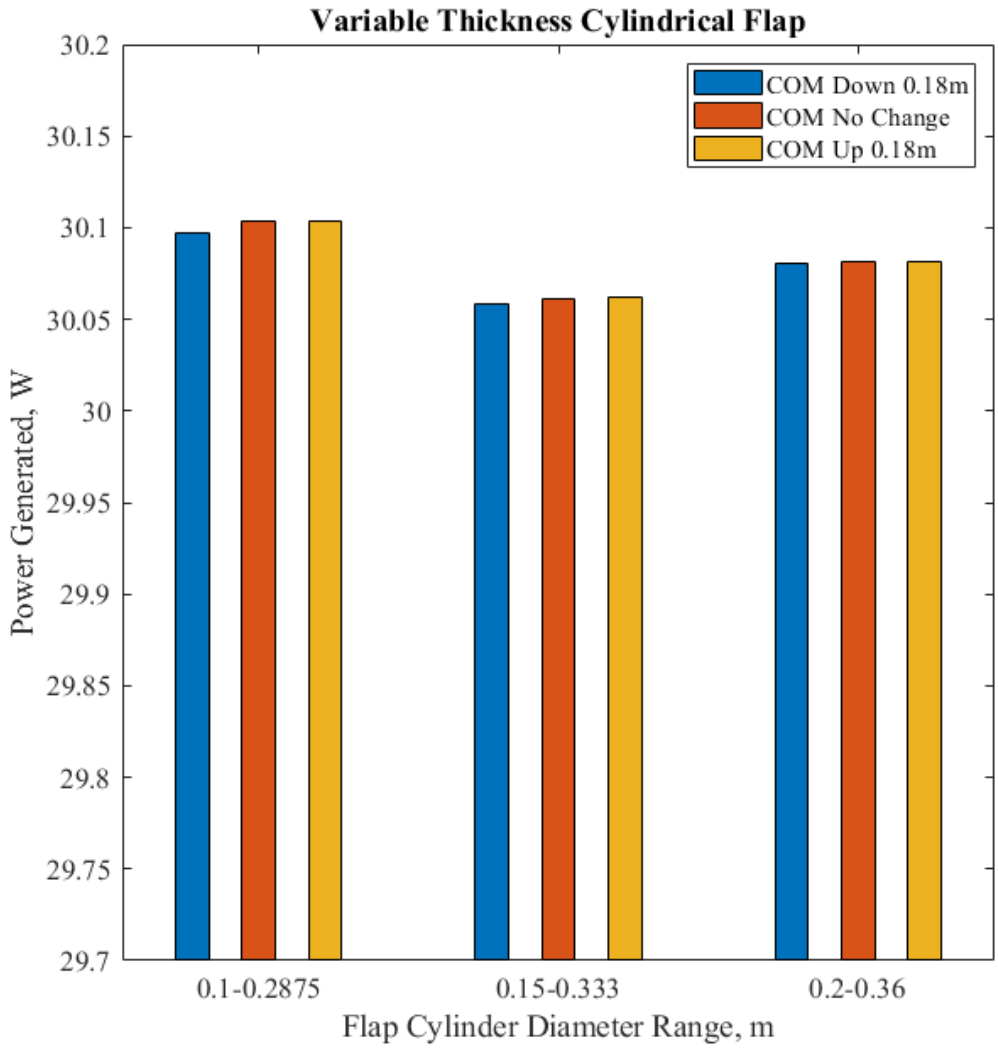

Figure 4.10: Variable Thickness Cylindrical Flap Power Output Over Different Cylinder Diameter Ranges and COMs.

The mean power generated for the variable thickness cylindrical flaps were the highest when the center of mass was translated up and the lowest when the center of mass was translated down for cylinder diameter ranges of 0.1-0.2875m and 0.15-0.333m. The power output increased by 0.00728W for a cylinder diameter range of 0.1-0.2875m and increased by 0.00381W for a cylinder diameter range of 0.15-0.333m as the center of mass was translated from the lowest to highest point. The mean power output was very close together for the

tests using a cylinder diameter range of 0.2-0.36m with a difference of 0.00094W between the lowest and middle center of mass values with the highest power generation at the middle center of mass value. The power output of the rectangular flap for the three centers of masses tested, with a data set for each tested density can be seen in Figure 4.11.

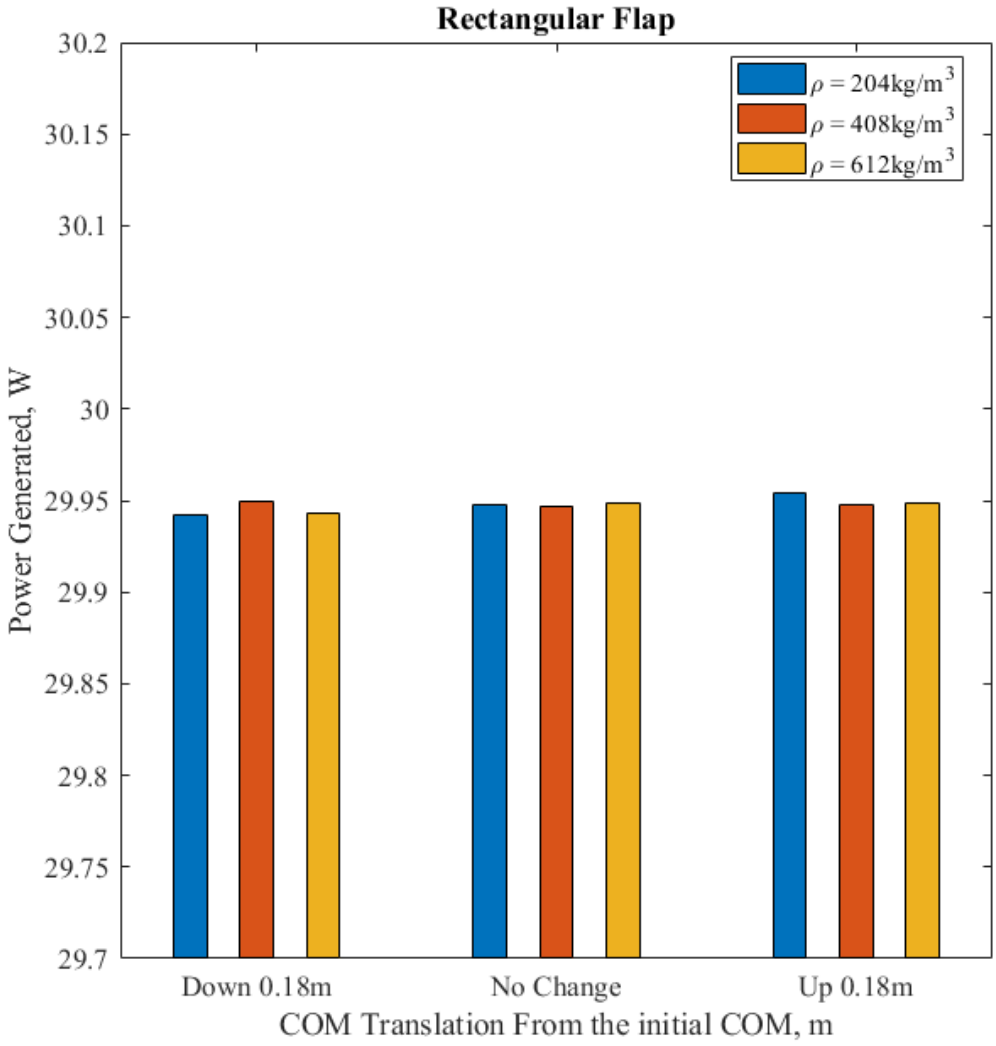

Figure 4.11: Rectangular Flap Power Output Over Different COMs and Densities.

The mean power data produced by the rectangular flap tests over different centers of mass and densities did not cause much variation. The highest mean power output came from the lowest density configuration and highest center of mass configuration with a value of 29.9542W and the lowest mean power output came from the lowest density configuration and the lowest center of mass configuration with a value of 29.942W. The power output of the curved surface flap for the three centers of masses tested, with a data set for each tested density can be seen in Figure 4.12.

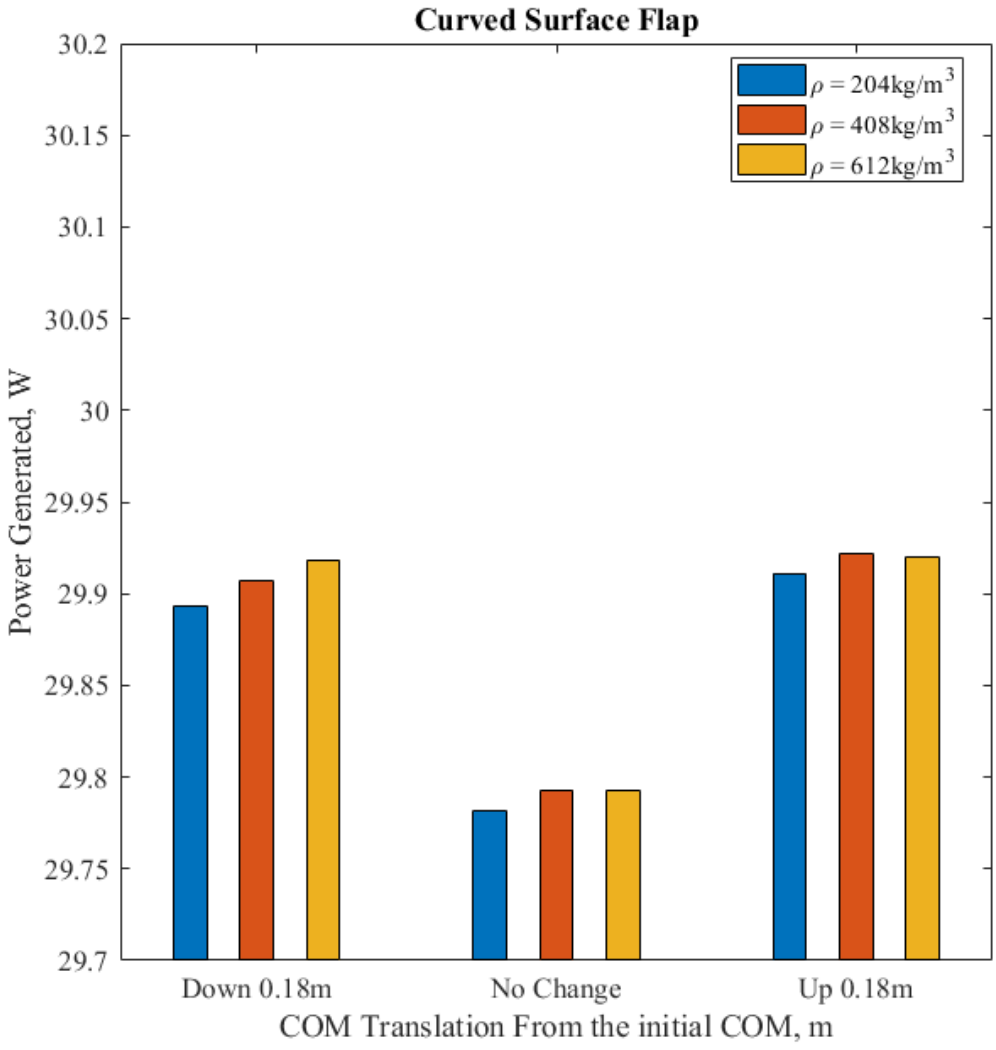

Figure 4.12: Curved Surface Flap Power Output Over Different COMs and Densities.

The mean power output from the curved surface flap had significantly lower values in the no change center of mass configurations compared to the translations up and down. Averaged across the tested densities, the generated power on the no change center of mass tests were 0.1171W lower than the lowest center of mass configuration and 0.1287W lower than the highest center of mass configuration. The lowest center of mass tests had the most variation of power generated between the tested densities with a change of 0.02548W between a density of $204kg/m^3$ and $612kg/m^3$. The power output of the variable thickness flap for the three centers of masses tested, with a data set for each tested density can be seen in Figure 4.13.

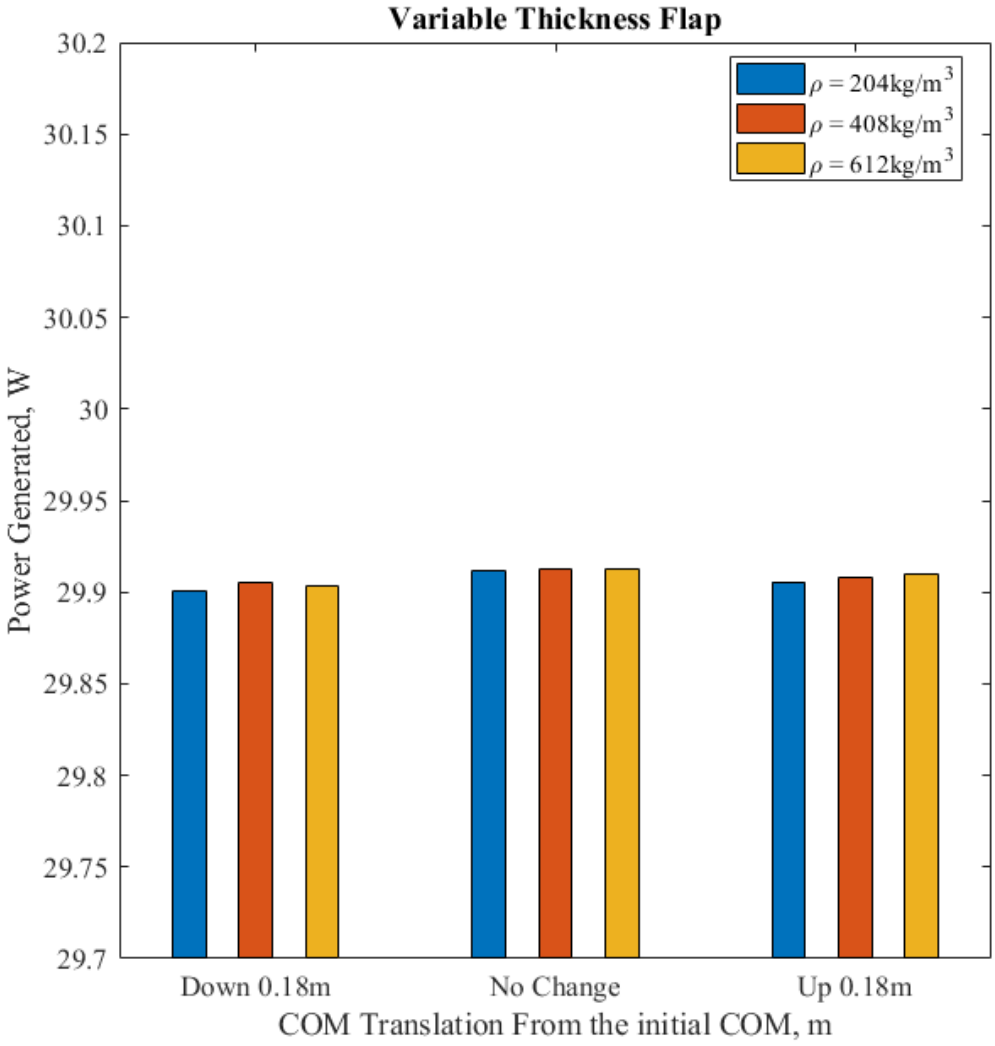

Figure 4.13: Variable Thickness Flap Power Output Over Different COMs and Densities.

The mean generated power from the variable thickness flap tests over different centers of mass and densities did not cause much variation. The highest power output from this data set came from the highest center of mass configuration and density configuration with a value of 29.9097W. The lowest mean power generated from this data set came from the lowest center of mass configuration and density configuration with a value of 29.9009W. The power output of the cylindrical flap for the three centers of masses tested, with a data set

for each tested density can be seen in Figure 4.14.

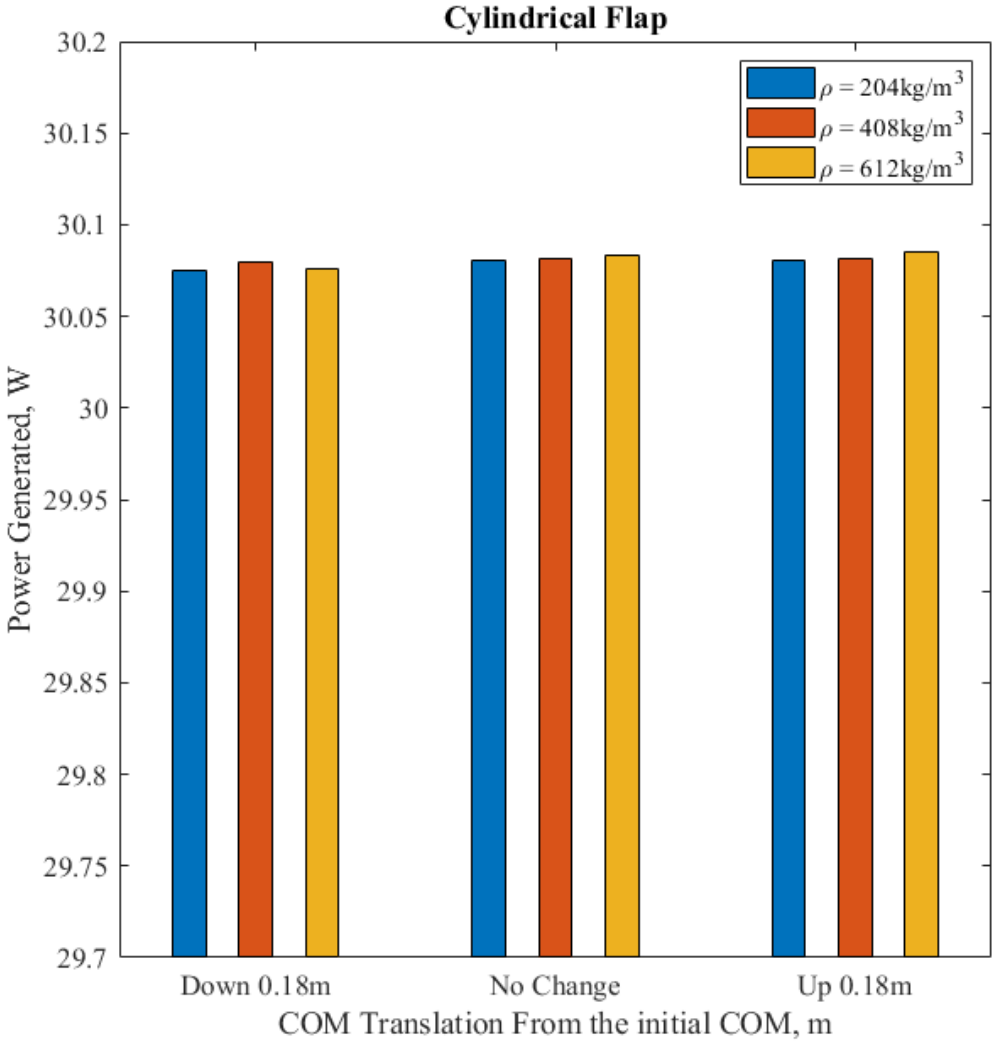

Figure 4.14: Cylindrical Flap Power Output Over Different COMs and Densities.

The mean power produced by the cylindrical flap tests over different centers of mass and densities had a very similar distribution to the variable thickness flap data shown in Figure 18 but translated up about 0.17W. The highest power output from this data set came from the highest center of mass configuration and density configuration with a value of 30.0855W. The lowest mean power generated from this data set came from the lowest center of mass

configuration and density configuration with a value of 30.0754W. The power output of the variable thickness cylindrical flap for the three centers of masses tested, with a data set for each tested density can be seen in Figure 4.15.

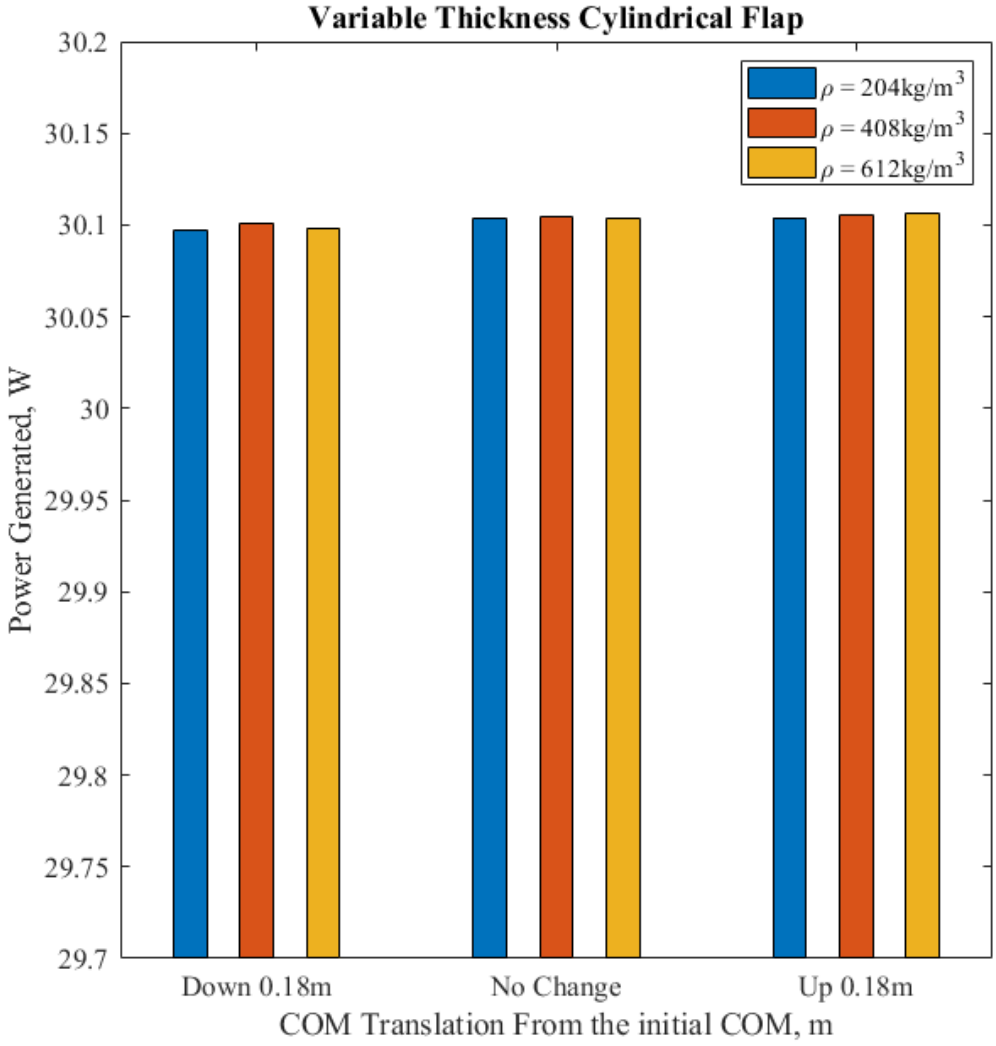

Figure 4.15: Variable Thickness Cylindrical Flap Power Output Over Different COMs and Densities.

The mean power outputs from the variable thickness cylindrical flap were all very similar for the different densities tested. For the center of mass moved down 0.18m, no change, and moved up 0.18m the average power generated across the density tests were 30.0987W, 30.1037W, and 30.1052W respectively. The highest difference in power generated across the density tests was in the lowest center of mass configuration with a change of 0.0044W. The power output of the flap shapes for the lowest density configuration and no change in the center of mass can be seen in Figure 4.16.

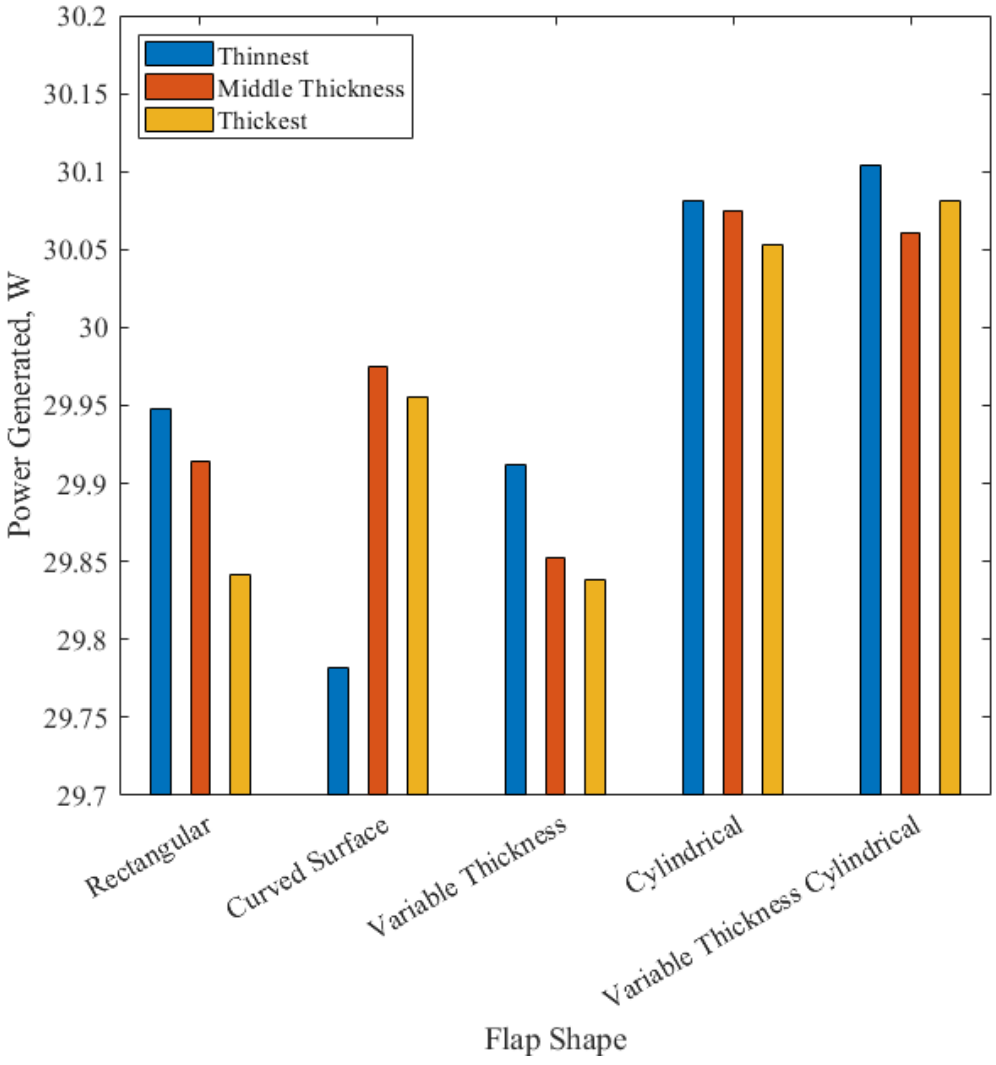

Figure 4.16: Flap Power Output Over Different Flap Shapes and Thicknesses.

The mean generated power was the highest for all of the shapes in the thinnest configuration except for the curved surface flap, which had the lowest mean power out of all tests with a value of 29.7814W. This value does not match the generated power of the same shape on the thicker variations; this could be due to an error in the creation/meshing of the shape or an error in simulations. The flap shape with the highest mean generated power was the variable thickness cylindrical flap on its thinnest configuration with a value of 30.1037W. Discounting the power output of the curved surface flap, the flap with the highest difference in power output between the thicknesses was the rectangular flap with a difference of 0.1068W. The variable thickness flap had the second highest mean power output difference with a value of 0.074W. The power output of the flap shapes for the lowest thickness configuration and no change in the center of mass can be seen in Figure 4.17.

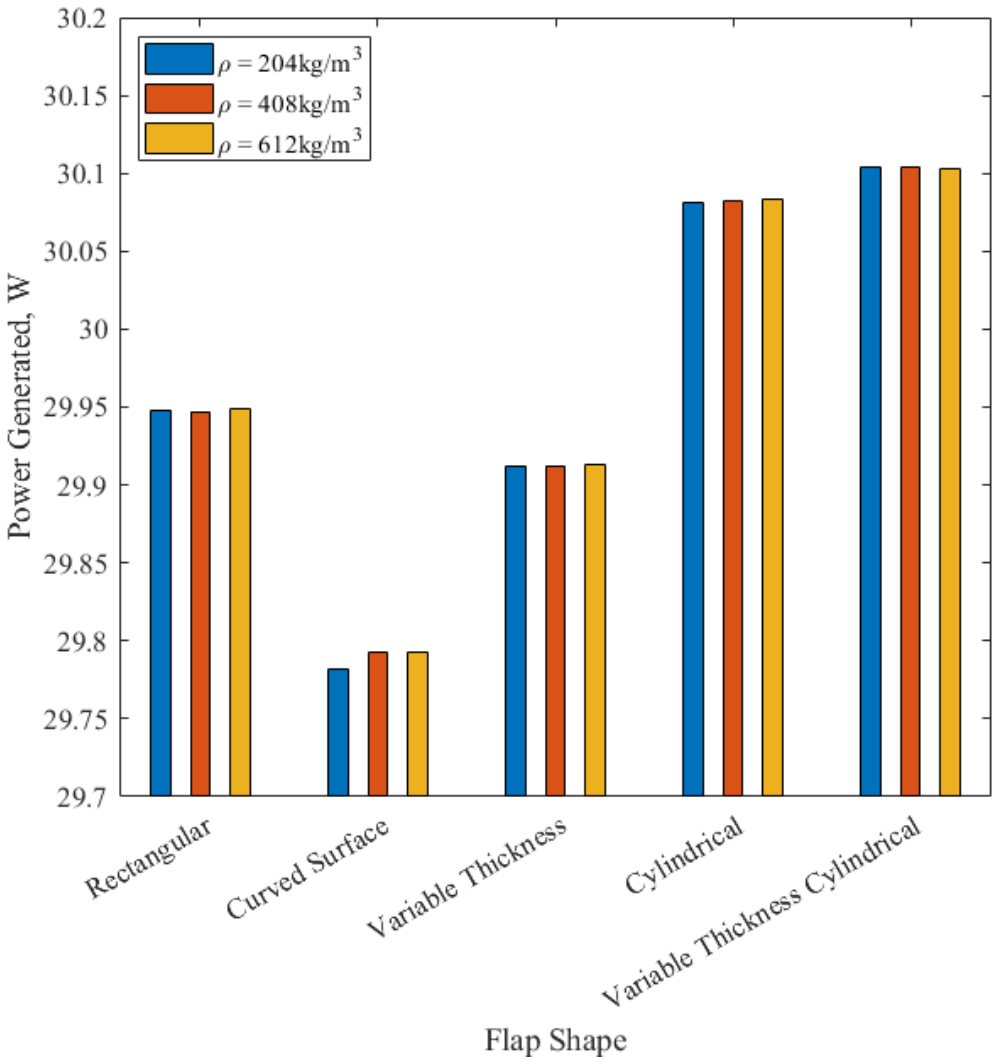

Figure 4.17: Flap Power Output Over Different Flap Shapes and Densities.

The mean power output across the shapes and tested densities did not follow a trend and there was little change in the mean power values when the density was changed for the same shape. Based on the tests shown in the above graph, the most to least efficient flap shapes are variable thickness cylindrical, cylindrical, rectangular, variable thickness, then curved surface. The respective mean powers generated averaged across the density tests are 30.1037W, 30.0819W, 29.9478W, 29.9125W, and 29.789W. One factor to note is that the

mean power generated for the curved surface flap for the second curve radius configuration has an average power output of 29.9762W and the third curve radius is slightly lower, so the first curve radius tests are likely outliers caused by an error during the simulation stage. The power output of the flap shapes for the lowest thickness configuration and the lowest density configuration can be seen in Figure 4.18.

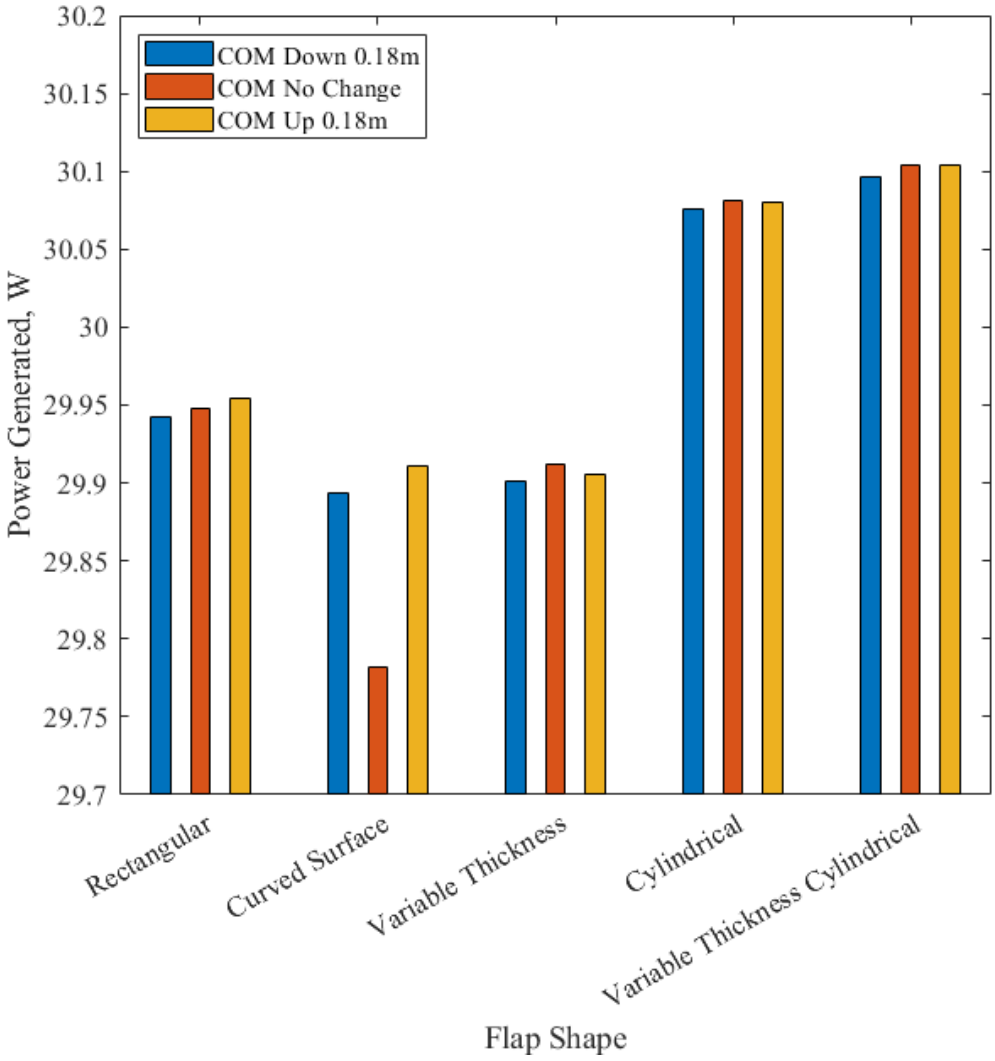

Figure 4.18: Flap Power Output Over Different Flap Shapes and COMs.

The mean power output across the shapes did not follow a trend as the center of mass was moved up and down, but the generated power results did vary more than the results from changing the flap density. The overall highest power output followed the same trend as in the density tests. Discounting the curved surface results, the flap shape with the highest difference in generated power was the rectangular flap with a difference of 0.0122W between the lowest and highest center of mass configurations.

In regard to PTO damping and stiffness, the simulations showed significant variation based on the flap shape. A trend that was followed by all of the flap shapes is that the higher the flap density, the higher the stiffness values would be to get the mean power output. The damping that produced the highest power output was not affected by the center of mass or density, only the thickness related variable. The magnitude of change varied between the shapes, but the thicker the flap, the higher the damping value that provided the maximum power. The mean power output for each flap shape with the configuration of each variable and the PTO damping and stiffness values can be seen in Table 4.1 below.

Table 4.1: Maximum Power Output for Each Shape and Variable Configuration

		Flap and PTO Variables				
Flap Shape	Maximum Power (W)	Thickness (m)	COM (m)	Density (kg/m^3)	Stiffness (Nm/rad)	Damping (Nsm/rad)
Rectangular	-29.95418913	0.05	Up 0.18	204	1500	12500
Curved Surface	-29.98878405	0.025	Up 0.18	612	1500	13000
Variable Thickness	-29.91298823	0.15-0.18	No Change	612	3000	15500
Cylindrical	-30.08553945	0.19375	Up 0.18	612	2500	16000
Variable Thickness Cylindrical	-30.10632594	0.1-0.2875	Up 0.18	612	3000	16500

Overall, the flaps made up of overlapping cylinders produced significantly more power than the other flap shapes, being the only two flap shapes that generated more than 30W. The next closest flap shape to 30W is the curved surface flap with a maximum generated power

of 29.989W. The flap shape was the variable that caused the most variation in generated power with differences up to 0.3W. The thickness related variable caused the next most power output differences and the changes to the center of mass and density caused minimal changes compared to the other variables. The effects of these variables are only true for the most efficient values for the PTO stiffness and damping coefficients.

4.2 Free Decay

The experimental free decay test results showed that the larger the initial angle, the lower the natural period. The only result that did not follow this trend was Static 5, this is likely because the water in the wave tank was not allowed to settle after moving the flap to its initial angle, so the rebounding waves interacted with the flap before the first oscillation was complete. The initial angles and natural periods of the five experimental tests "Static 1-5" can be seen in Table 4.2.

Table 4.2: Experimental Free Decay Initial Angles and Natural Periods

Experimental Test	**Initial Angle (Degrees)**	**Natural Period (Seconds)**
Static 1	8.07	7.15
Static 2	8.08	6.88
Static 3	10.25	6.72
Static 4	12.93	6.67
Static 5	18.17	7.04
	Delta (1-4)	0.48

The angular position over time for the experimental tests can be seen in Figure 4.19. The raw data looked noisy and had a lot of overlapping data because the sensor on the flap took a measurement every 0.01s and it was very sensitive to any changes in flap angle. The raw data was modified to remove some of the noise by averaging the values to follow the trend of the angles while still using all of the recorded data points. The modified data can be seen in Figure 4.20. It can be seen that the flap was able to rotate back and forth one time before

the angular position is displaced from the standard decay due to the waves bouncing back off of the far end of the wave tank. Possible improvements for future tests to reduce the impact of the wave rebound are to wait longer for the water to settle before releasing the flap or to use a larger wave tank so it takes longer for the waves to reach the flap.

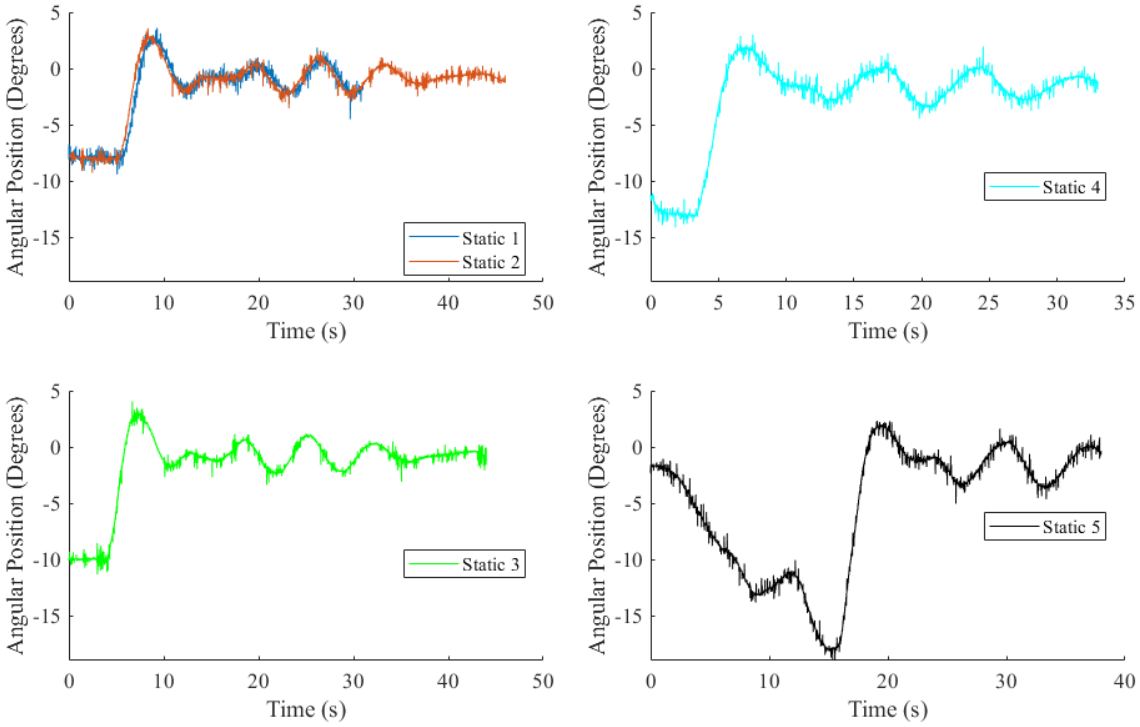

Figure 4.19: Raw Experimental Free Decay Angular Position Over Time.

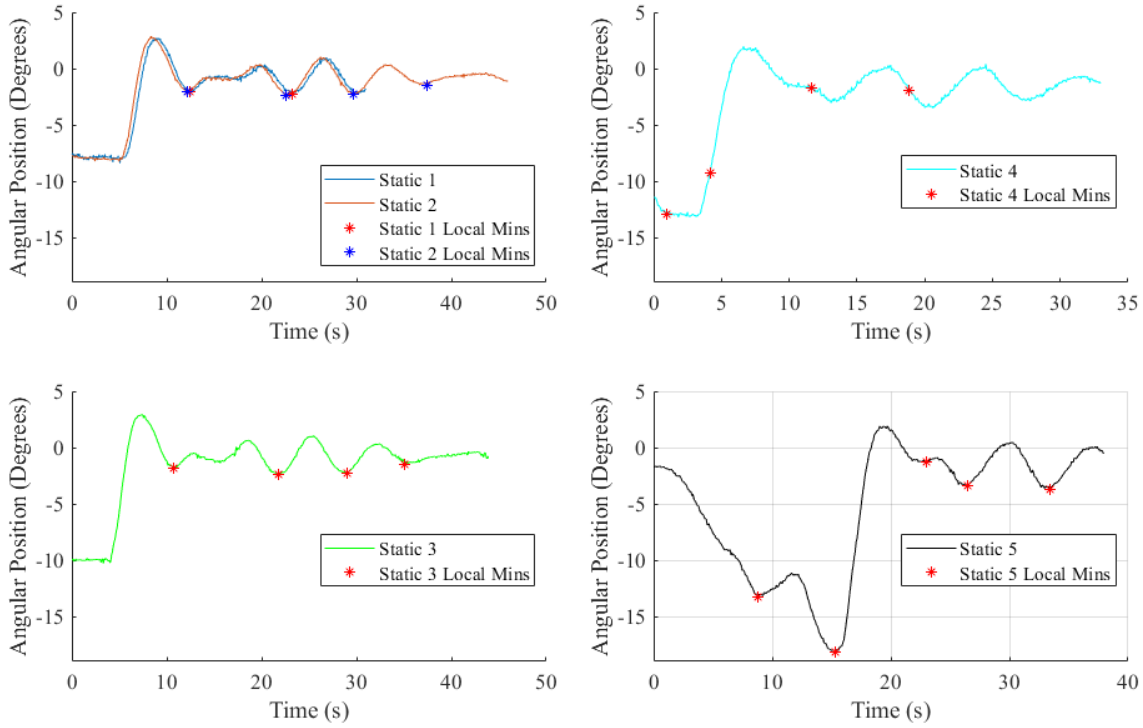

Figure 4.20: Filtered Experimental Free Decay Angular Position Over Time.

The initial angles from the experimental tests were used for the numerical tests; the natural periods of the experimental tests can be compared to the natural periods of the numerical tests using the results in Table 4.3. The numerical free decay test results showed minimal differences in the natural period over different initial angular positions, though they followed the trend in the experimental results that higher initial angles reduce the natural period.

Table 4.3: Numerical Rectangular Flap and Experimental Free Decay Natural Periods

Initial Angle (Degrees)	**Rect1**	**Rect2**	**Rect3**	**Experimental**
8.07	7.686	5.298	4.396	7.15
8.08	7.686	5.298	4.396	6.88
10.25	7.684	5.297	4.395	6.72
12.93	7.682	5.296	4.394	6.67
18.17	7.675	5.291	4.391	7.04
Average Period (s):	7.682	5.296	4.394	6.892
Delta (s):	0.011	0.007	0.005	0.48

The factors that impacted the natural periods the most were the mass and geometric properties. The larger flaps with more mass oscillated significantly faster than the lighter, smaller flaps. Table 4.4 compares the mass properties of the flap used in the experimental test to the simulated rectangular flaps.

Table 4.4: Numerical Rectangular Flap and Experimental Free Decay Natural Periods

Flap	**Mass** (kg)	**Moments of Inertia** [**Ixx Iyy Izz**] ($kg \times m^2$)			**Density** (kg/m^3)	**Thickness** (m)	**Volume** (m^3)
Wave Tank	32.588	4.561	7.342	11.777	194.48	0.112	0.168
Rect1	18.063	5.467	2.133	3.342	204	0.05	0.0885
Rect2	46.839	13.802	5.423	8.512	204	0.133	0.230
Rect3	73.913	21.187	8.468	13.261	204	0.217	0.362

The mass of the experimental flap falls between the simulated flaps Rect1 and Rect2; using the correlation between the flap mass and natural period, it would be expected that the experimental flap natural periods fall between that of Rect1 and Rect2. Another difference between the numerical and experimental free decay tests is that the numerical tests follow exponential decay and are not affected by any water rebound caused by the flap moving. One of the numerical free decay tests can be seen in Figure 4.21.

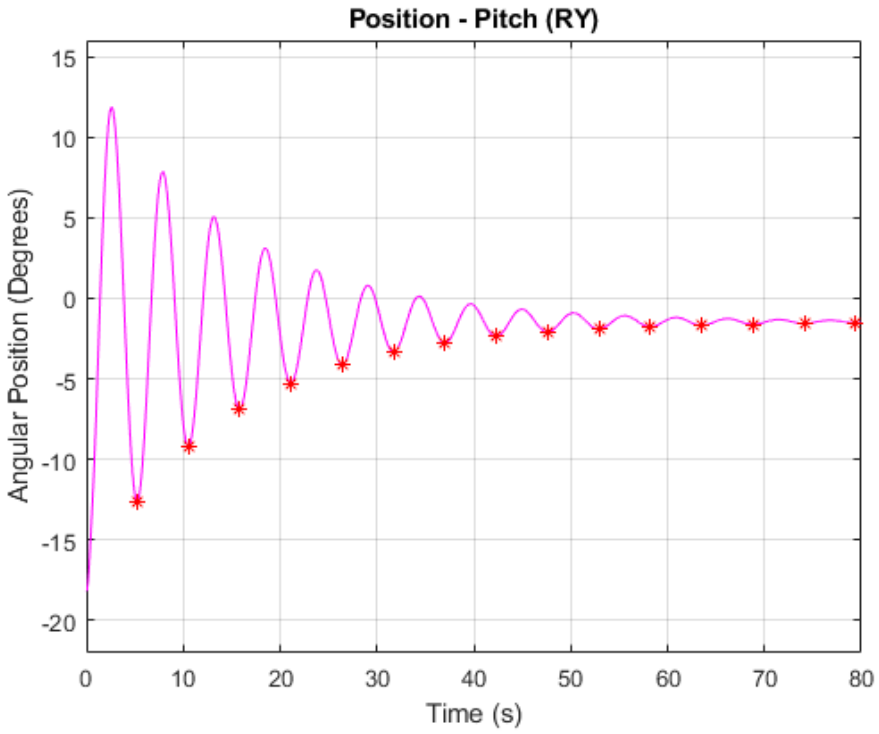

Figure 4.21: Numerical Flap Decay, $\theta = 18.17°$.

The numerical and experimental free decay results were plotted together to compare the angular position and natural periods, this can be seen in Figure 4.22. The three groups of solid lines represent the three rectangular flaps Rect1, Rect2, and Rect3. Rect1 had the longest set of natural periods of the numerical results and Rect3 had the shortest set of natural periods of the numerical results. The return of the experimental flaps from the initial angle to zero at the beginning follow the trend between the masses, such that the experimental results are between Rect1 and Rect2. It can be seen that the wave rebound during the highest two initial angle tests affected the angular position between 7 and 8 seconds after the flap was released while the response of the three smaller angle tests were affected between 9 and 10 seconds after the flap was released.

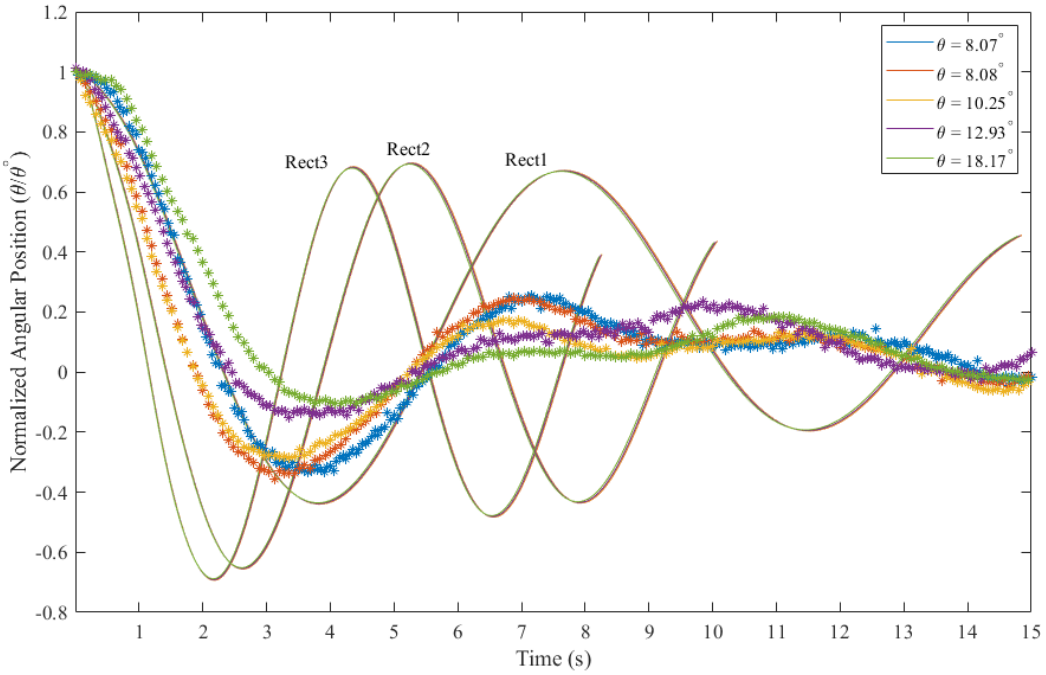

Figure 4.22: Numerical (Solid) and Experimental (Starred) Flap Decay Variable Volume Tests.

As the volume of the simulated flaps decreased, the natural period of oscillation increased. All of the tested numerical flaps had a uniform density of $204kg/m^3$ and the experimental flap had a density of $194.48kg/m^3$. The Rect1 flap had the lowest volume of the flaps used in free decay tests with a value of $0.0885m^3$ and it had an average natural period of $7.683s$. The experimental flap had the next lowest volume of $0.168m^3$ with an average natural period of $6.892s$. Rect2 had a volume of $0.230m^3$ with an average natural period of $5.296s$ and Rect3 had a volume of $0.362m^3$ with an average natural period of $4.394s$. Two other factors affecting the natural period were the mass and density of the flaps. All of the numerical flaps in the initial tests had a density of $204kg/m^3$ and the experimental flap had a density of $194.48kg/m^3$. A second series of free decay tests were conducted with the different density configurations of Rect2 to get the natural periods with respect to mass and density. Rect2 was chosen because it has the closest volume of the simulated flaps to the experimental flap,

with a difference of $0.062m^3$. The results can be seen in Figure 4.23.

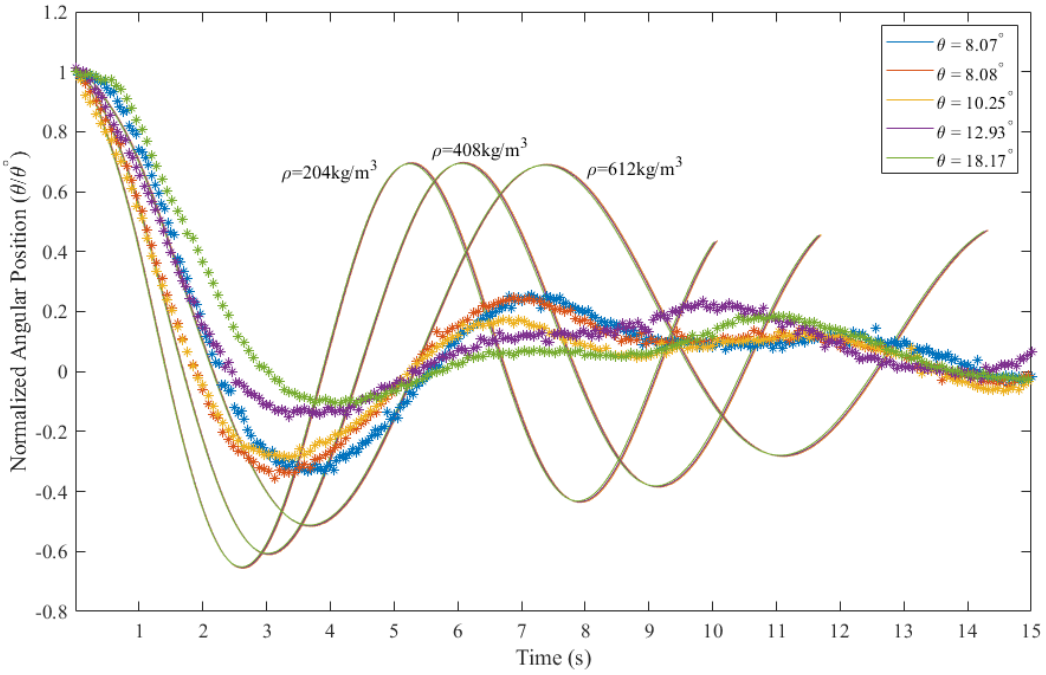

Figure 4.23: Rect2 Numerical (Solid) and Experimental (Starred) Flap Decay Variable Density Tests.

As the density of the numerical flaps increased, so did the natural period of oscillation. The three tests all used the geometry of Rect2 with a volume of $0.230m^3$ and the mass increased with the density. The mean natural periods for the flaps from lowest to highest densities were $5.296s$, $6.111s$, and $7.415s$, respectively. The time it took the flaps to reach the first minimum angle were all similar and fell between $2.5s$ and $3.5s$. The large difference between the different experimental test natural periods can be attributed to the rebound of the waves bouncing off of the wave tank before one period was completed. The natural periods of Rect2 over different density values and the experimental natural periods can be seen in Table 4.5 below.

Table 4.5: Numerical Rectangular Flap and Experimental Free Decay Natural Periods

Initial Angle (Degrees)	**Rect2Dens1**	**Rect2Dens2**	**Rect2Dens3**	**Experimental**
8.07	5.298	6.113	7.418	7.15
8.08	5.298	6.113	7.418	6.88
10.25	5.297	6.112	7.417	6.72
12.93	5.296	6.11	7.415	6.67
18.17	5.291	6.106	7.409	7.04
Average Period (s):	5.296	6.111	7.415	6.892
Delta (s):	0.007	0.007	0.009	0.480

A third series of free decay tests were conducted with the different density configurations of Rect1 because the natural periods of the initial free decay tests for that flap thickness most closely follow the natural periods of the experimental flap results. The results of these tests can be seen in Figure 4.24.

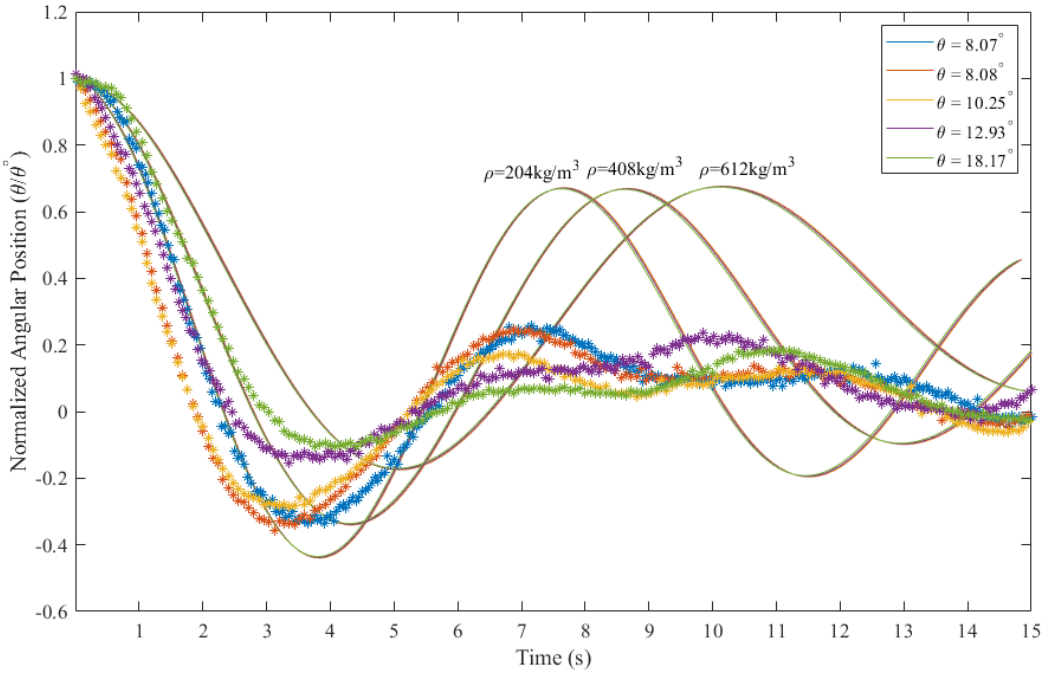

Figure 4.24: Rect1 Numerical (Solid) and Experimental (Starred) Flap Decay Variable Density Tests.

As the density of the numerical flaps increased, so did the natural period of oscillation. The three tests all used the geometry of Rect1 with a volume of $0.089m^3$ and the mass increased with the density. The mean natural periods for the flaps from lowest to highest densities were $7.683s$, $8.676s$, and $10.163s$, respectively. The time it took the flaps to reach the first minimum angle fell between $3.5s$ and $5s$. The ratio of the angular position compared to the initial angular position was the most similar between the numerical and experimental tests when using a density of $408kg/m^3$ but the time the free decay reached the lowest point was the most similar when using a density of $204kg/m^3$. The natural periods of Rect1 over different density values and the experimental natural periods can be seen in Table 4.6 below.

Table 4.6: Numerical Rectangular Flap and Experimental Free Decay Natural Periods

Initial Angle (Degrees)	**Rect1Dens1**	**Rect1Dens2**	**Rect1Dens3**	**Experimental**
8.07	7.686	8.68	10.171	7.15
8.08	7.686	8.68	10.171	6.88
10.25	7.684	8.678	10.167	6.72
12.93	7.682	8.674	10.161	6.67
18.17	7.675	8.666	10.146	7.04
Average Period (s):	7.683	8.676	10.163	6.892
Delta (s):	0.011	0.014	0.025	0.480

As the density of the flap increased, so did the amount of change between the natural periods as the initial angles increased. This occurred in the tests with Rect2 as well, but the effects were more significant in the tests with Rect1. The lower volume of Rect1 compared to Rect2 increased overall, but the rate it increased was significantly larger than in the Rect2 tests.

Chapter 5

Conclusion

Five flap shapes for an OSWEC were introduced and tested over multiple variables to determine the configuration with the highest power output. The flap shape is the variable that has the most significant effects on the power output. The thickness-related variable had a considerable trend with the thinnest flap configurations produced the most power. The center of mass changes had minimal impact on the power output and results for each shape were dependent on the other variables. The density of the flap also had minimal effects on the power output of the WEC, but it followed a trend in which the configurations with the highest tested density provided the highest power output. The flap configuration that produced the most power with a value of $30.106W$ was the variable thickness cylindrical flap with the highest cylinder diameter range, center of mass translated up by $0.18m$, and the highest tested density of $612kg/m^3$.

Chapter 6

Future Work

In the future, an avenue of research that would be beneficial to support current results is to complete more experimental free decay tests. Ideally these tests would be completed in a wave tank that is longer, so the flap has more time to complete a full period before the waves interfere with the natural free decay. In the current experimental tests, only the first few seconds of angular position data could be used before the water bounced back and changed the natural frequency of the flap response. It would also be of interest to complete simulations using an exact representation of the experimental flap rather than only flaps of similar shape, mass, and density. Completing simulations with an exact replica of the experimental flap would significantly reduce the variables that could cause the natural periods to be different between the numerical and experimental results. A tertiary course of action that should be taken when using these results for physical flap design is to complete an economic analysis. It would be worthwhile to determine the costs of materials in relation to the different variables that were manipulated on each flap design and if the improvements to the generated power are worth the costs to build the device.

References

[1] Water facts - worldwide water supply | ARWEC| CCAO | area offices | california-great basin | bureau of reclamation.

[2] Gualbert H.P Oude Essink. Improving fresh groundwater supply—problems and solutions. 44(5):429–449.

[3] Ibrahim Dincer. Renewable energy and sustainable development: a crucial review. 4(2):157–175.

[4] B Drew, A R Plummer, and M N Sahinkaya. A review of wave energy converter technology. 223(8):887–902.

[5] K Gunn and C Stock-Williams. Quantifying the potential global market for wave power.

[6] Gunnar Mork, Stephen Barstow, Alina Kabuth, and M. Teresa Pontes. Assessing the global wave energy potential. In *29th International Conference on Ocean, Offshore and Arctic Engineering: Volume 3*, pages 447–454. ASMEDC.

[7] Johannes Falnes. A review of wave-energy extraction. 20(4):185–201.

[8] B. Czech and P. Bauer. Wave energy converter concepts : Design challenges and classification. 6(2):4–16.

[9] Emiliano Renzi, Jack Leech, and Iain Phillips. WEC-GA optimisation tool for an oscillating wave surge converter. page 7.

[10] M. Leijon, O. Danielsson, M. Eriksson, K. Thorburn, H. Bernhoff, J. Isberg, J. Sundberg, I. Ivanova, E. Sjöstedt, O. Ågren, K.E. Karlsson, and A. Wolfbrandt. An electrical approach to wave energy conversion. 31(9):1309–1319.

[11] Arthur Pecher, Jens Peter Kofoed, and Tommy Larsen. Design specifications for the hanstholm WEPTOS wave energy converter. 5(4):1001–1017.

[12] N Sharmila, P Jalihal, A Swamy, and M Ravindran. Wave powered desalination system. 29(11):1659–1672.

[13] Pasquale Contestabile and Diego Vicinanza. Coastal defence integrating wave-energy-based desalination: A case study in madagascar. 6(2):64.

[14] Matt Folley, Baltasar Peñate Suarez, and Trevor Whittaker. An autonomous wave-powered desalination system. 220(1):412–421.

[15] Koray Senol and Mehdi Raessi. Enhancing power extraction in bottom-hinged flap-type wave energy converters through advanced power take-off techniques. 182:248–258.

[16] A. Garcia-Teruel and D.I.M. Forehand. A review of geometry optimisation of wave energy converters. 139:110593.

[17] Nathan Tom, Michael Lawson, Yi-Hsiang Yu, and Alan Wright. Preliminary analysis of an oscillating surge wave energy converter with controlled geometry: Preprint.

[18] Adi Kurniawan and Torgeir Moan. Optimal geometries for wave absorbers oscillating about a fixed axis. 38(1):117–130.

[19] Milad Shadman, Segen F. Estefen, Claudio A. Rodriguez, and Izabel C.M. Nogueira. A geometrical optimization method applied to a heaving point absorber wave energy converter. 115:533–546.

[20] N.M. Tom, M.J. Lawson, Y.H. Yu, and A.D. Wright. Development of a nearshore oscillating surge wave energy converter with variable geometry. 96:410–424.

[21] Emiliano Renzi and F. Dias. Resonant behaviour of an oscillating wave energy converter in a channel. 701:482–510.

[22] Wan-chao Zhang, Heng-xu Liu, Liang Zhang, and Xue-wei Zhang. Hydrodynamic analysis and shape optimization for vertical axisymmetric wave energy converters. 30(6):954–966.

[23] Louis Papillon, Ronan Costello, and John V. Ringwood. Boundary element and integral methods in potential flow theory: a review with a focus on wave energy applications. 6(3):303–337.

[24] Yi-Hsiang Yu, Ye Li, Kathleen Hallett, and Chad Hotimsky. Design and analysis for a floating oscillating surge wave energy converter. In *Volume 9B: Ocean Renewable Energy*, page V09BT09A048. American Society of Mechanical Engineers.

[25] Jeremiah Pastor and Yucheng Liu. Frequency and time domain modeling and power output for a heaving point absorber wave energy converter. 5(2):101.

[26] Michael Lawson, Braulio Barahona Garzon, Fabian Wendt, Yi-Hsiang Yu, and Carlos Michelen. COER hydrodynamic modeling competition: Modeling the dynamic response of a floating body using the WEC-sim and FAST simulation tools. In *Volume 9: Ocean Renewable Energy*, page V009T09A005. American Society of Mechanical Engineers.

[27] Kelley Ruehl, Carlos Michelen, Yi-Hsiang Yu, and Michael Lawson. Update on WEC-sim validation testing and code development.

[28] Bret Bosma, Asher Simmons, Pedro Lomonaco, Kelley Ruehl, and Budi Gunawan. WEC-sim phase 1 validation testing: Experimental setup and initial results. In *Volume 6: Ocean Space Utilization; Ocean Renewable Energy*, page V006T09A025. American Society of Mechanical Engineers.

[29] Kelley Ruehl, Dominic D. Forbush, Yi-Hsiang Yu, and Nathan Tom. Experimental and numerical comparisons of a dual-flap floating oscillating surge wave energy converter in regular waves. 196:106575.

[30] Rhino user's guide - introduction.

[31] WEC-sim.

Chapter 7

Appendix

7.1 WEC-Sim Mechanics Explorer

The WEC-Sim mechanics explorer can be seen in Figure 7.1.

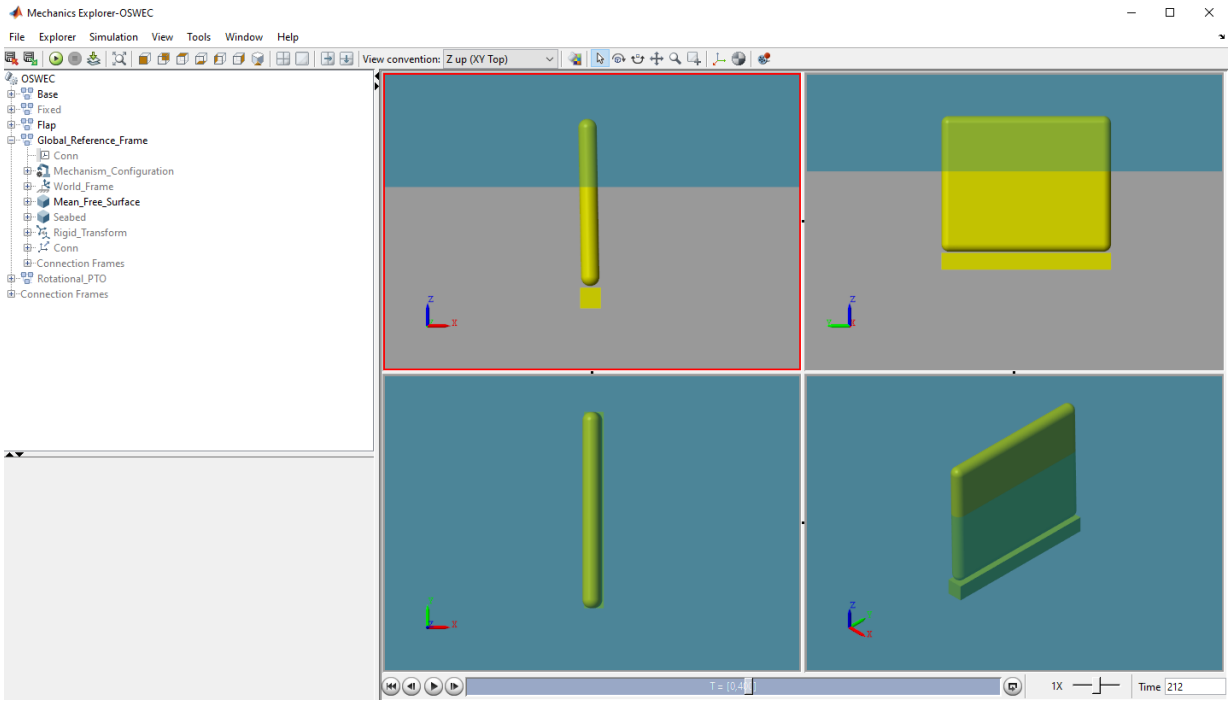

Figure 7.1: WEC-Sim Mechanics Explorer.

7.2 Flap Drawings for Each Shape

The thickness related variable refers to the variable on the x-axis, the dimension in the right view of the part. The flap width refers to the variable on the y-axis, which is the horizontal direction on the front and top views of the part. The flap height refers to the variable along the z-axis, which is the vertical direction on the front and right views of the part.

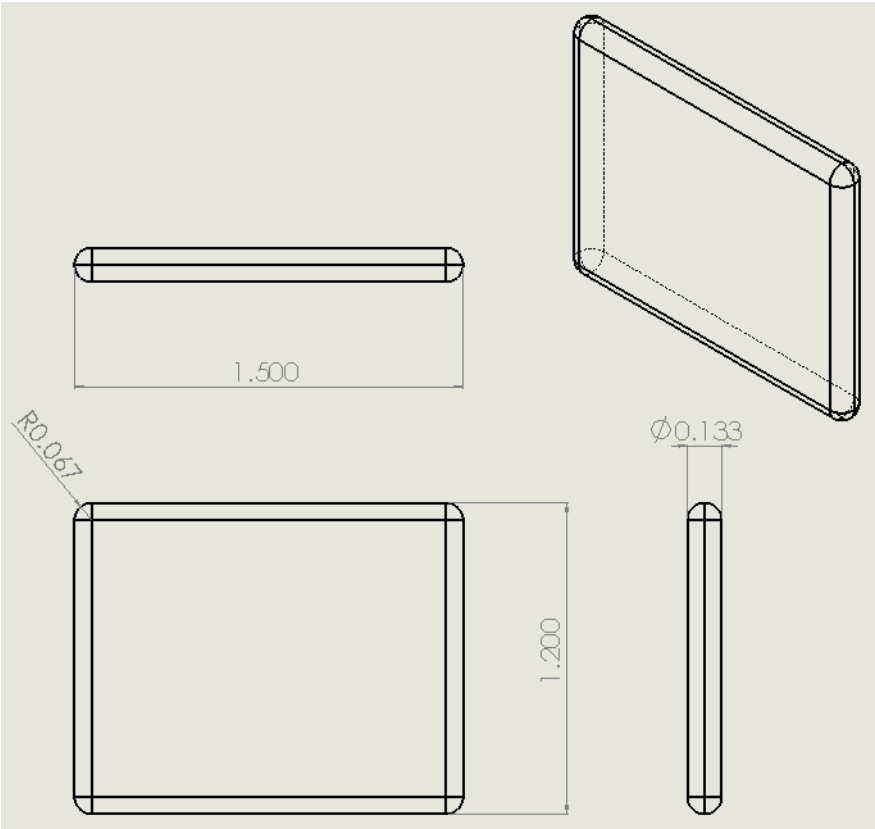

Figure 7.2: Rectangular Flap Drawing.

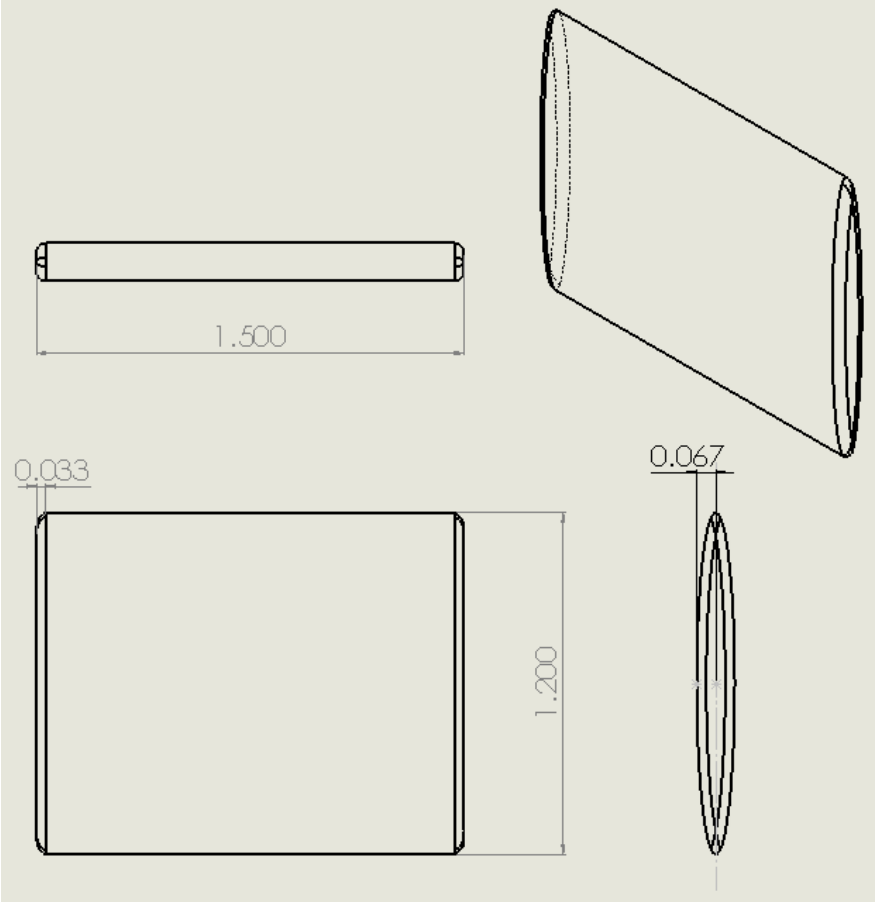

Figure 7.3: Curved Surface Flap Drawing.

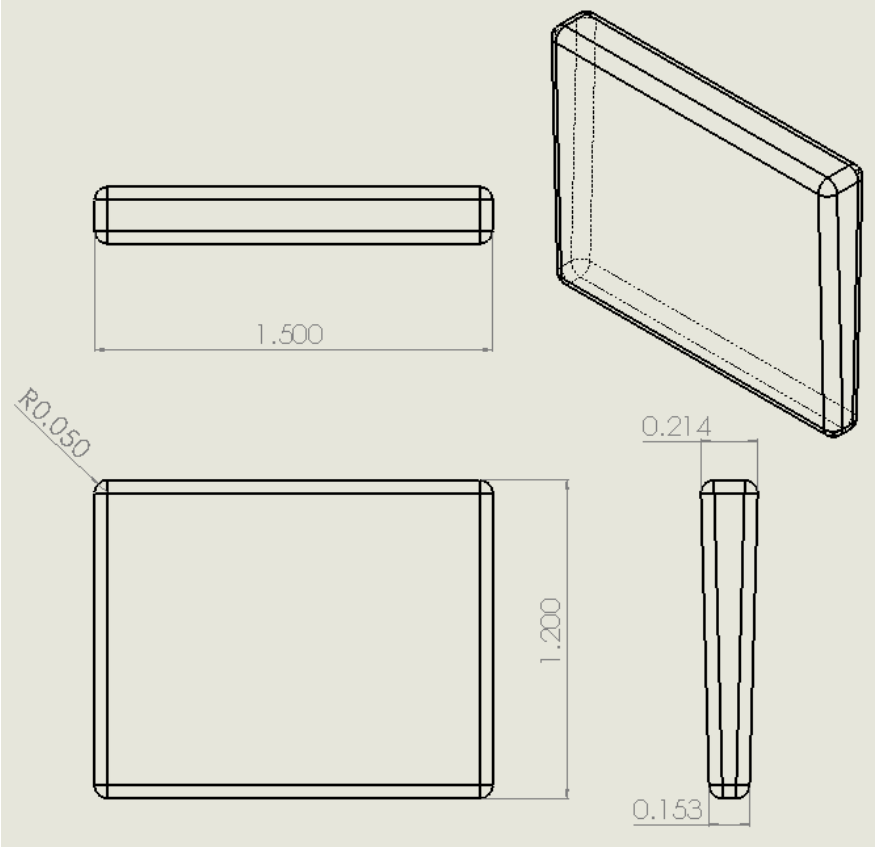

Figure 7.4: Variable Thickness Flap Drawing.

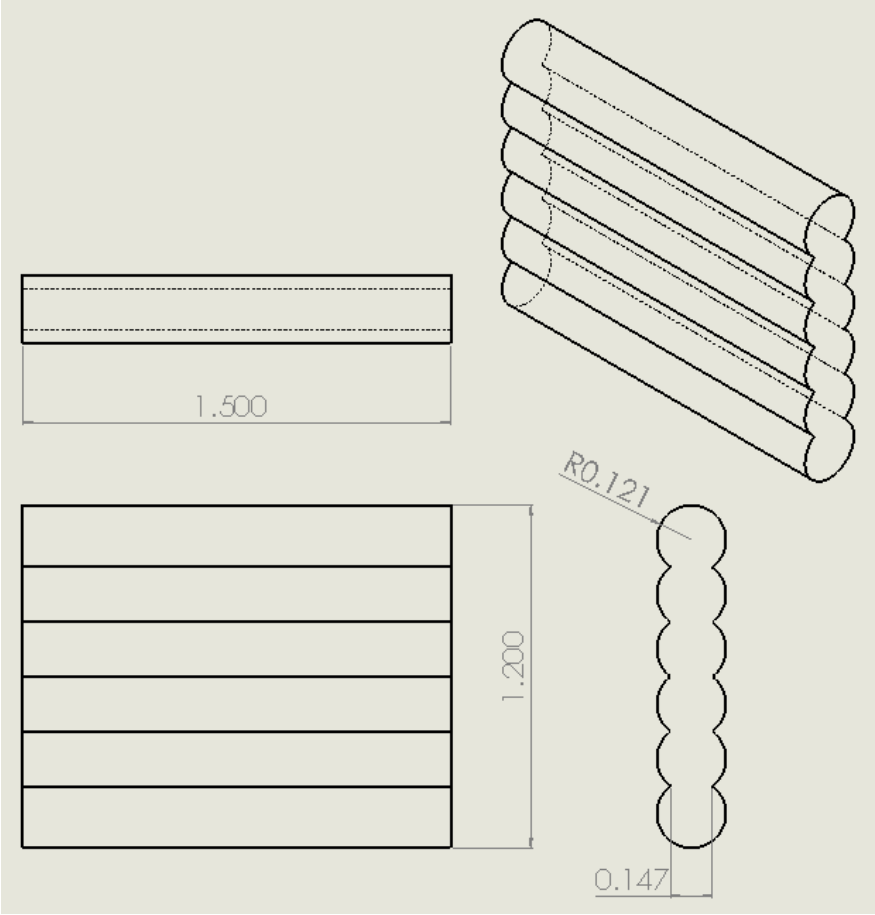

Figure 7.5: Cylindrical Flap Drawing.

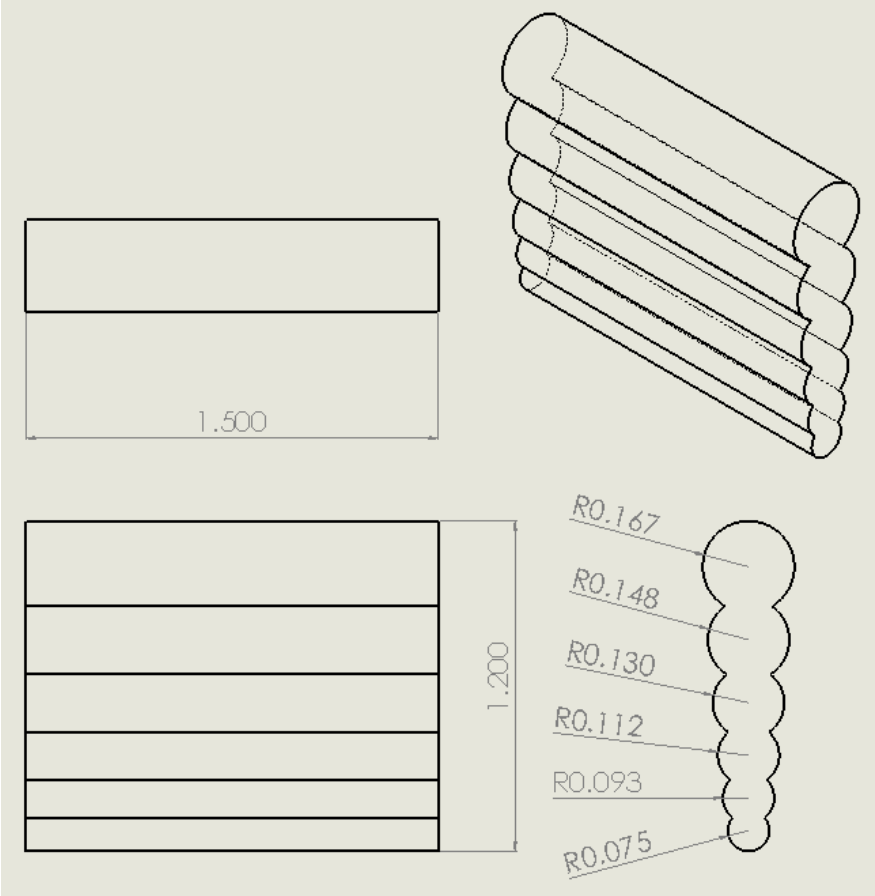

Figure 7.6: Variable Thickness Cylindrical Flap Drawing.

7.3 Flap Meshes for Each Shape

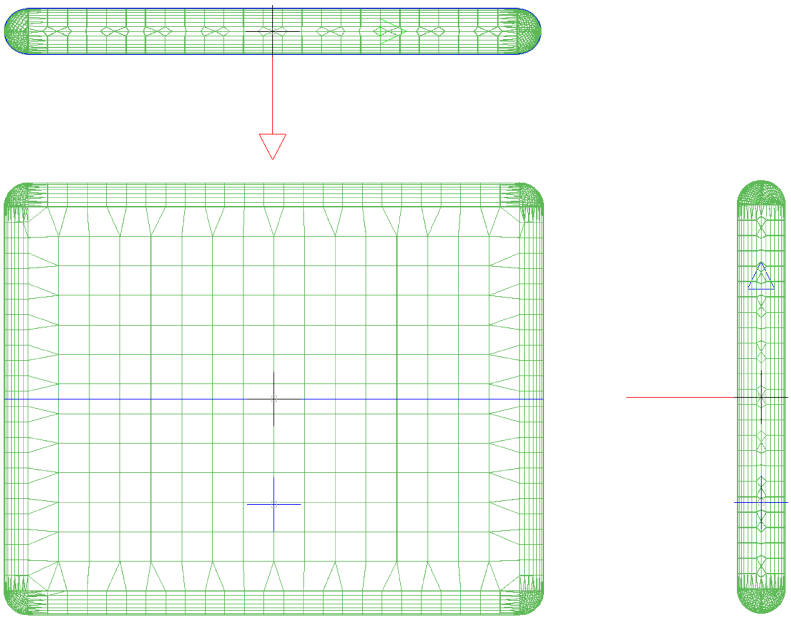

Figure 7.7: Rectangular Flap Mesh.

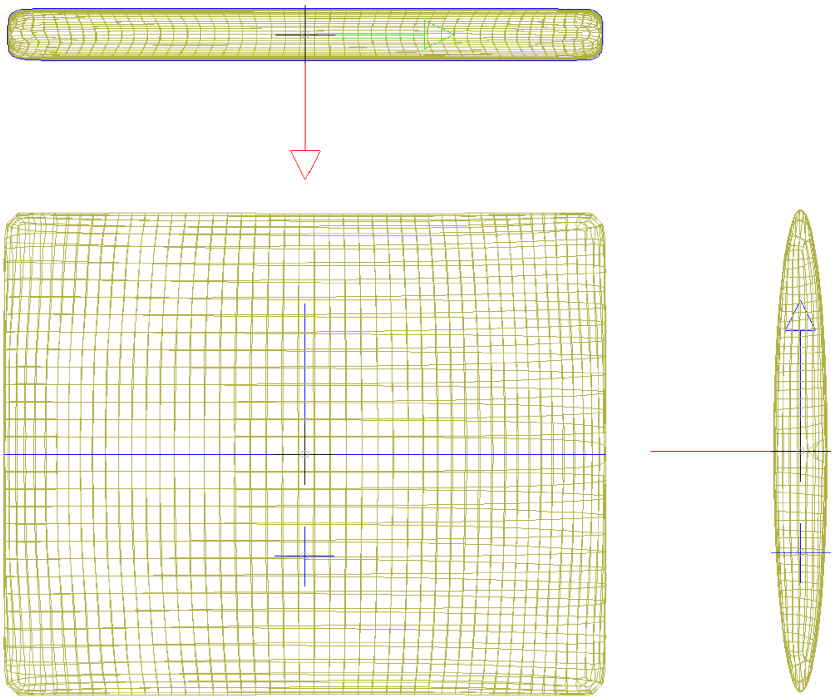

Figure 7.8: Curved Surface Flap Mesh.

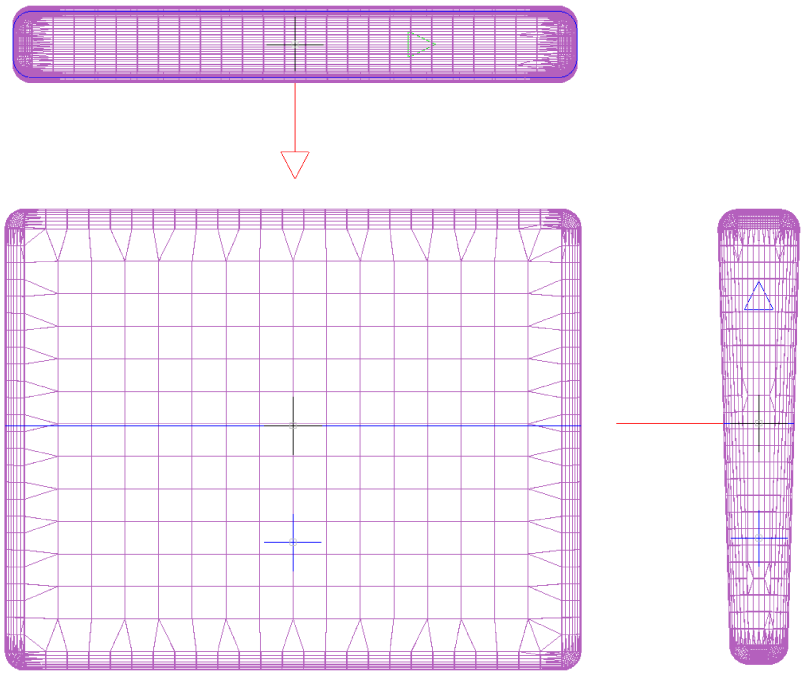

Figure 7.9: Variable Thickness Flap Mesh.

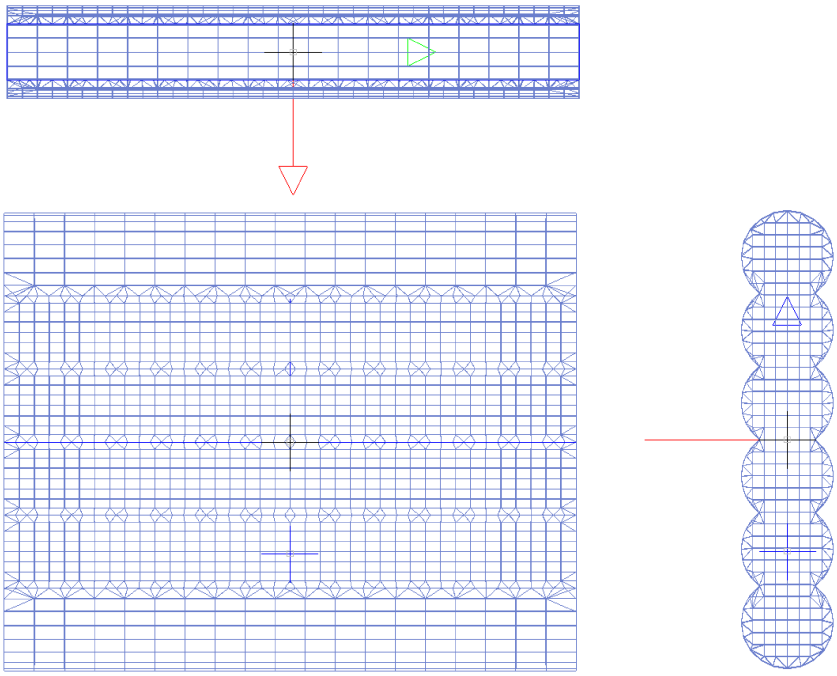

Figure 7.10: Cylindrical Flap Mesh.

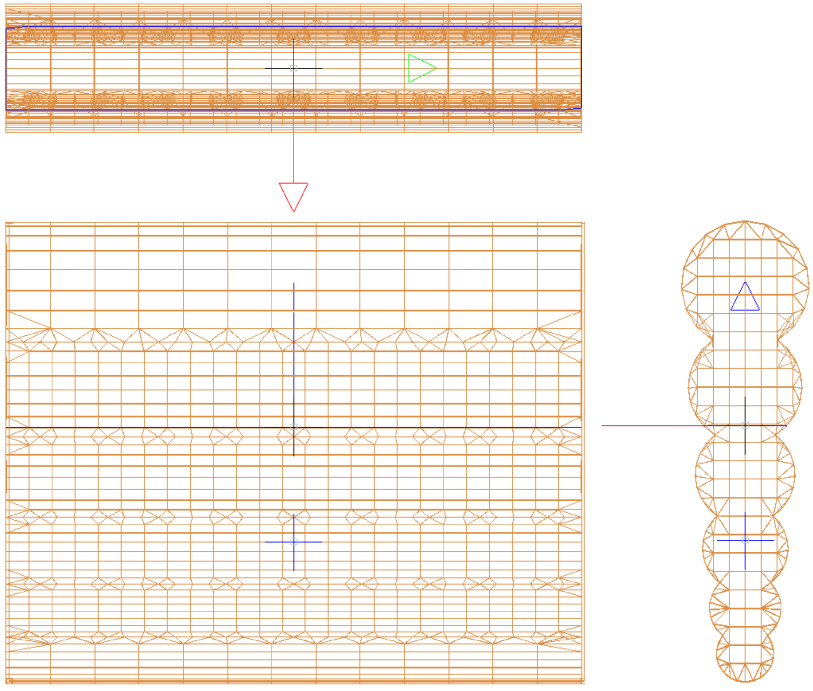

Figure 7.11: Variable Thickness Cylindrical Flap Mesh.